Chapter 1

INTERACTION OF PLANETARY NEBULAE , ETA-CARINAE AND SUPERNOVA REMNANTS WITH THE INTERSTELLAR MEDIUM

Lorenzo Zaninetti [*]
Dipartimento di Fisica Generale, Via Pietro Giuria 1, 10125 Torino,

Abstract

The image of planetary nebulae (PN), supernova remnant (SNR) and Eta-Carinae is made by three different physical processes. The first process is the expansion of the shell that can be modeled by the canonical laws of motion in the spherical case and by the momentum conservation when gradients of density are present in the interstellar medium. The quality of the simulations is introduced along one direction as well along many directions. The second process is the diffusion of particles that radiate from the advancing layer. The 3D diffusion from a sphere , the 1D diffusion with drift and 1D random walk are analyzed. The third process is the composition of the image through an integral operation along the line

[*]Email address: zaninetti@ph.unito.it

of sight. The developed framework is applied to three PN which are A39 , the Ring nebula and the etched hourglass nebula MyCn 18, the hybrid object Eta-Carinae , and to two SNR which are SN 1993J and SN 1006. In all the considered cases a careful comparison between the observed and theoretical profiles in intensity is done.

1.   Introduction

The spherical explosion in galactic astrophysics models two different objects:

- The planetary nebula (PN) that are characterized by small terminal velocities of the order of few km/s and small energy , E, released in the expansion , $E \approx 10^{42}$ erg.

- The supernova remnant (SNR) that are characterized by high velocities $\approx 5000 km/s$ and high energy involved , $E \approx 10^{51}$ erg.

These two main classifications does not cover peculiar astrophysical objects such as the nebula around η-Carinae which is characterized by high velocity , $\approx 300 \ km/s$ and low energy involved , $E \approx 10^{39}$ erg. We now summarize the existing models on these three astrophysical objects. **PN** The PN rarely presents a circular shape generally thought to be the projection of a sphere on the sky. In order to explain the properties of PN, [1] proposed the interacting stellar wind (ISW) theory. Later on [2] proposed the two wind model and the two phase model. More often various types of shapes such as elliptical , bipolar or cigar are present, see [3–8]. The bipolar PNs , for example , are explained by the interaction of the winds which originate from the central star , see [9–12]. Another class of models explains some basic structures in PNs through hydrodynamical models, see [13, 14] or through self-organized magnetohydrodynamic (MHD) plasma configurations with radial flow, see [15]. An attempt to make a catalog of line profiles using various shapes observed in real PNs was done by [16]. This ONLINE atlas , available at
http://132.248.1.102/Atlas_profiles/img/, is composed of 26 photo-ionization models corresponding to 5 geometries, 3 angular density laws and 2 cavity sizes, four velocity fields for a total of 104 PNs, each of which can be observed from 3 different directions. [17] suggest that a planetary nebula is formed and evolves by the interaction of a fast wind from a central star with a slow wind from its progenitor , an Asymptotic Giant Branch (AGB) star.

η-**Carinae**   The nebula around η-Carinae was discovered by [18] and the name "the Homunculus" arises from the fact that on the photographic plates it resembled a small plump man, see [19]. More details on the various aspects of η-Carinae can be found in [20]. The structure of the Homunculus Nebula around η-Carinae has been analyzed with different models, we cite some of them:

- The shape and kinematics is explained by the interaction of the winds expelled by the central star at different injection velocities, see [9].

- The possibility that the nebulae around luminous blue variables (LBVs) are shaped by interacting winds has been analyzed by [21]. In this case a density contrast profile of the form $\rho = \rho_0(1 + 5\cos^4 \Theta)$ was used where Θ is the angle to the equatorial plane.

- The origin and evolution of the bipolar nebula has been modeled by a numerical two-dimensional gasdynamic model where a stellar wind interacts with an aspherical circumstellar environment, see [10].

- Cooling models form ballistic flows (that is, a pair of cones each with a spherical base) whose lateral edges become wrinkled by shear instabilities, see [22].

- The scaling relations derived from the theory of radiatively driven winds can model the outflows from luminous blue variable (LBV) stars, taking account of stellar rotation and the associated latitudinal variation of the stellar flux due to gravity darkening. In particular for a star rotating close to its critical speed, the decrease in effective gravity near the equator and the associated decrease in the equatorial wind speed results naturally in a bipolar, prolate interaction front, and therefore in an asymmetric wind, see [23].

- Two oppositely ejected jets inflate two lobes (or bubbles) representing a unified model for the formation of bipolar lobes, see [24, 25].

- A two-dimensional, time-dependent hydrodynamical simulation of radiative cooling, see [26].

- Launch of material normal to the surface of the oblate rotating star with an initial kick velocity that scales approximately with the local escape speed, see [27].

- A 3D model of wind-wind collision for X-ray emission from a supermassive star, see [28].

- Two-dimensional hydrodynamical simulations of the eruptive events of the 1840s (the great outburst) and 1890s (the minor outburst), see [29].

SNR The study of the supernova remnant (SNR) started with [30] where an on ongoing collisional excitation as a result of a post-explosion expansion of the SNR against the ambient medium was suggested. The next six decades where dedicated to the deduction of an analytical or numerical law of expansion. The target is a relationship for the instantaneous radius of expansion, R, of the type $\propto t^m$ where t is time and m is a parameter that depends on the chosen model. On adopting this point of view, the Sedov expansion predicts $R \propto t^{0.4}$, see [31], and the thin layer approximation in the presence of a constant density medium predicts $R \propto t^{0.25}$, see [32]. A simple approach to the SNR evolution in the first 10^4 yr assumes an initial free expansion in which $R \propto t$ until the surrounding mass is of the order of 1 $M_\odot$ and a second phase characterized by the energy conservation in which according to the Sedov solution $R \propto t^{2/5}$, see [33]. A third phase characterized by an adiabatic expansion with $R \propto t^{2/7}$ starts after 10^4 yr, see [33]. A more sophisticated approach given by [34, 35] analyzes self-similar solutions with varying inverse power law exponents for the density profile of the advancing matter, R^{-n}, and ambient medium, R^{-s}. The previous assumptions give a law of motion $R \propto t^{\frac{n-3}{n-s}}$ when $n > 5$. Another example is an analytical solution suggested by [36] where the radius–time relationship is regulated by the decrease in density: as an example, a density proportional to R^{-9} gives $R \propto t^{2/3}$. With regard to observations, the radius–time relationship was clarified when a decade of

very-long-baseline interferometry (VLBI) observations of SN 1993J at wavelengths of 3.6, 6, and 18 cm became available, see [37–39]. As a first example, these observations collected over a 10 year period can be approximated by a power law dependence of the type $R \propto t^{0.82}$. This observational fact rules out the Sedov model and the momentum conservation model. In this paper we describe in Section 2. the observed morphologies of PNs, SNRs and $\eta - car$. Section 3. analyzes five different laws of motion that model the spherical and aspherical expansion and Section 4. applies the various law of motion to well defined astrophysical objects introducing the quality of the simulation. Section 5. reviews old and new formulas on diffusion , Section 6. reviews the existing situation with the radiative transport equation and Section 7. contains detailed information on how to build an image of the astrophysical objects here considered.

2. Astrophysical Objects

This section presents the astronomical data of a nearly spherical PN known as A39, a weakly asymmetric PN , the Ring nebula , and a bipolar PN which is the etched hourglass nebula MyCn 18 . The basic data of η-Carinae which is not classified as a PN due to the high velocities observed are also reported. The section ends with two SNR , the symmetric SN 1993J and the weakly asymmetric SN 1006 .

2.1. A circular PN , A39

The PN A39 is extremely round and therefore can be considered an example of spherical symmetry, see for example Figure 1 in [40] . In A39 the radius of the shell , R_{shell} is

$$R_{shell} = 2.42 \times 10^{18}\Theta_{77}D_{21} \, cm = 0.78 \, pc \quad , \tag{1}$$

where Θ_{77} is the angular radius in units of $77''$ and D_{21} the distance in units of 2.1 kpc , see [40] . The expansion velocity has a range $[32 \leftrightarrow 37 \, \frac{km}{s}]$ according to [41] and the age of the free expansion is 23000 yr, see [40]. The angular thickness of the shell is

$$\delta \, r_{shell} = 3.17 \, 10^{17}\Theta_{10}D_{21}cm = 0.103 \, pc \quad , \tag{2}$$

where Θ_{10} is the thickness in units of $10.1''$ and the height above the galactic plane is $1.42 \, kpc$, see [40]. The radial distribution of the intensity in $[OIII]$ image of A39 after subtracting the contribution of the central star is well described by a spherical shell with a $10''$ rim thickness, see Figure 1 and [40].

2.2. A weakly asymmetric PN , M57

The Ring nebula , also known as M57 or NGC6720 , presents an elliptical shape characterized by a semi-major axis of $42''$, a semi-minor axis of $29.4''$ and ellipticity of 0.7, see Table I in [42]. The distance of the Ring nebula is not very well known ; according to [43] the distance is 705 pc . In physical units the two radii are

$$R_{shell,minor} = 0.1\Theta_{29.4}D_{705} \, pc \qquad semi-minor \, radius$$
$$R_{shell,major} = 0.14\Theta_{42}D_{705} \, pc \qquad semi-major \, radius \quad , \tag{3}$$
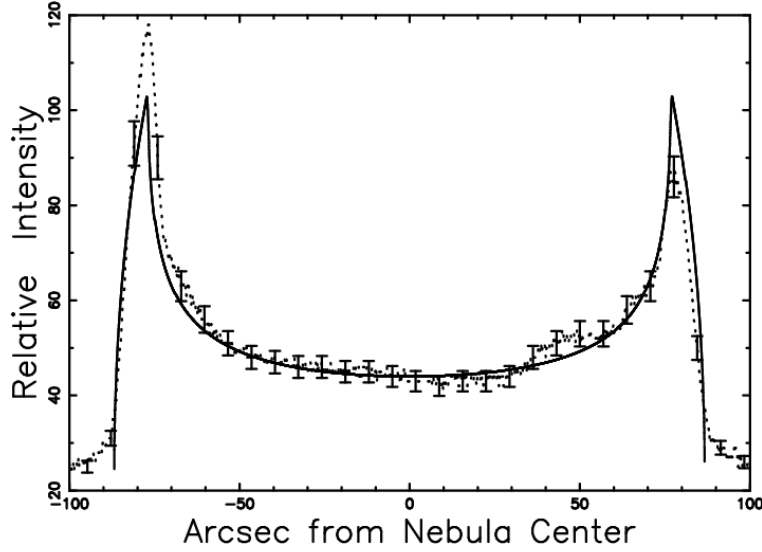
Figure 1.   Cut of the relative intensity of the PN A39 crossing the center in the east-west direction (dotted line with some error bar) and the rim model (full line) fully described in Jacoby et al. (2001) .

where $\Theta_{29.4}$ is the angular minor radius in units of $29.4''$, Θ_{42} is the angular major radius in units of $42''$ and D_{705} the distance in units of $705\ pc$. The radial velocity structure in the Ring Nebula was derived from observations of the H_2 (molecular Hydrogen) v = 1-0 S(1) emission line at $2.122\ \mu m$ obtained by using a cooled Fabry- Perot etalon and a near-infrared imaging detector , see [42] . The velocity structure of the Ring Nebula covers the range $\left[-30.3 \leftrightarrow 48.8\ \frac{km}{s}\right]$.

2.3.   A strongly asymmetric PN , MyCn 18

MyCn 18 is a PN at a distance of 2.4 kpc and clearly shows an hourglass-shaped nebula, see [44,45]. On referring to Table 1 in [46] we can fix the equatorial radius in $2.80 \times 10^{16}\ cm$, or $0.09\ pc$, and the radius at $60°$ from the equatorial plane $3.16 \times 10^{17}\ cm$ or $0.102\ pc$. The determination of the observed field of velocity of MyCn 18 varies from an overall value of $10\ \frac{km}{s}$ as suggested by the expansion of $[OIII]$, see [45] , to a theoretical model by [46] in which the velocity is $9.6\ \frac{km}{s}$ when the latitude is 0 ° (equatorial plane) to $40.9\ \frac{km}{s}$ when the latitude is 60 °.

2.4.   Homunculus nebula

The star η-Carinae had a great outburst in 1840 and at the moment of writing presents a bipolar shape called the Homunculus, its distance is 2250 pc, see [47]. A more refined classification distinguishes between the large and little Homunculus, see [48]. The Homunculus has been observed at different wavelengths such as the ultraviolet and infrared by [20,49],
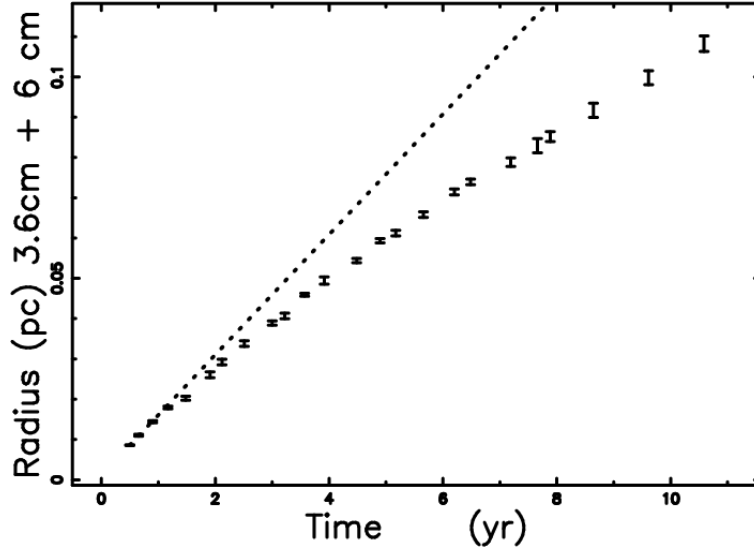
Figure 2. Radius in pc versus year of the SNR SN 1993J with vertical error bars. The em bands are $\lambda = 3.6\,cm$ and $\lambda = 6\,cm$. The data are extracted from Table 1 in Marcaide et al. 2009. The dotted line represents an expansion at a constant velocity.

x-ray by [50], $[FeII]\lambda 16435$ by [51], ammonia by [52], radio-continuum by [48], near-infrared by [53] and scandium and chromium lines by [54].

Referring to Table 1 in [55], we can fix the major radius at 22014 AU (0.106 pc) and the equatorial radius at 2100 AU (0.01 pc). The expansion velocity rises from $\approx\ 93\ km/s$ at the equator to $\approx\ 648\ km/s$ in the polar direction, see Table 1 and Figure 4 in [55]. The thickness of the H_2 shell is roughly $2 - 3\%$ of the polar radius, see [55].

2.5.   A circular SNR, SN 1993J

The supernova SN 1993J started to be visible in M81 in 1993, see [56], and presented a circular symmetry for 4000 days, see [37]. Its distance is 3.63 Mpc (the same as M81), see [57]. The expansion of SN 1993J has been monitored in various bands over a decade and Figure 2 reports its temporal evolution.

The observed instantaneous velocity decreases from $v = 15437\ \frac{km}{s}$ at $t = 0.052$ yr to $v = 8474\ \frac{km}{s}$ at $t = 10.53$ yr. We briefly recall that [58] quote an inner velocity from the shapes of the lines of $\approx 7000\frac{km}{s}$ and an outer velocity of $\approx 10000\frac{km}{s}$.

2.6.   A weakly asymmetric SNR, SN 1006

The diameter of the known remnants spans the range from 3 pc to 60 pc and attention is fixed on SN 1006 which started to be visible in 1006 AD and its possible diameter of 12.7 pc, see [59] . More precisely, on referring to the radio–map of SN 1006 at 1370 MHz by [60], it can be observed that the radius is greatest in the north–east direction. From the radio-map previously mentioned we can extract the following observed radii, $R = 6.8\ pc$ in the

polar direction and $R = 5.89\ pc$ in the equatorial direction. Information on the thickness of emitting layers is contained in a recent study by [61] which analyzes Chandra observations (i.e., synchrotron X-rays) from SN 1006 . The observations found that sources of non-thermal radiation are likely to be thin sheets with a thickness of about 0.04 pc upstream and 0.2 pc downstream of the surface of maximum emission, which coincide with the locations of Balmer-line optical emission , see [62] . The high resolution XMM-Newton Reflection Grating Spectrometer (RGS) spectrum of SN 1006 gives two solutions for the O VII triplet. One gives a shell velocity of 6500 km/s and the second one a shell velocity of 9500 km/s, see [63]. The value here adopted for the magnetic field can be $H = 10\mu\ Gauss$ as suggested by [61].

3.   Law of motion

This Section presents three solutions for the law of motion that describe a symmetric expansion. The momentum conservation is then applied in cases where the density of the interstellar medium is not constant but regulated by exponential or power law behavior.

3.1.   Spherical Symmetry - Power law solution

The equation of the expansion of the SNR can be modeled by a power law of the type

$$R(t) = R_0 (\frac{t}{t_0})^\alpha \quad , \tag{4}$$

where R is the radius of the expansion, t is the time , R_0 is the radius at $t = t_0$ and α an exponent which can be found from the numerical analysis. In the case of SN 1993J we have α =0.828 , R_0=0.0087 pc and t_0 = 0.498 yr

3.2.   Spherical Symmetry - Sedov solution

The momentum conservation is applied to a conical section of radius R with a solid angle $\Delta\ \Omega$, in polar coordinates, see [33]

$$\frac{d}{dt}(\Delta M R) = \Delta F \,, \tag{5}$$

where

$$\Delta M = \int_0^R \rho(R, \theta, \phi) dV \,, \tag{6}$$

is the mass of swept–up interstellar medium in the solid angle $\Delta\ \Omega$, ρ the density of the medium , P the interior pressure and the driving force:

$$\Delta\ F = PR^2 \Delta\Omega \,. \tag{7}$$

After some algebra the Sedov solution is obtained, see [31, 33]

$$R(t) = \left(\frac{25}{4} \frac{E\,t^2}{\pi\,\rho} \right)^{1/5} \quad , \tag{8}$$

where E is the energy injected in the process and t the time.

Another slightly different solution is formula (7.56) in [32]

$$R(t) = \left(\frac{25}{3} \frac{E\, t^2}{\pi\, \rho} \right)^{1/5} \quad , \tag{9}$$

where the difference is due to the adopted approximations.

Our astrophysical units are: time (t_4), which is expressed in 10^4 yr units; E_{42}, the energy in 10^{42} erg; and n_0 the number density expressed in particles cm^{-3} (density $\rho = n_0$m, where m=1.4m_{H}). With these units equation (8) becomes

$$R(t) \approx 0.198 \left(\frac{E_{42}\, t_4^2}{n_0} \right)^{1/5} pc \quad . \tag{10}$$

The expansion velocity is

$$V(t) = \frac{2}{5} \frac{R(t)}{t} \quad , \tag{11}$$

which expressed in astrophysical units is

$$V(t) \approx 7.746 \frac{\sqrt[5]{E_{42}}}{\sqrt[5]{n_0}\, t_4^{\,3/5}} \frac{km}{s} \quad . \tag{12}$$

Equations (10) and (12) represent a system of two equations in two unknowns : t_4 and E_{42}. By inserting for example $R = 0.78\,pc$ in equation (10) we find

$$t_4 = 77.15 \frac{1}{\sqrt{E_{42}}} \quad , \tag{13}$$

and inserting $V = 35\ km\ s^{-1}$ in equation (12) we obtain

$$0.3954 \sqrt{E_{42}} = 35 \quad . \tag{14}$$

The previous equation is solved for $E_{42} = 7833.4$ that according to equation (13) means t_4=.87173. These two parameters allows a rough evaluation of the mechanical luminosity $L = \frac{E}{t}$ that turns out to be $L \approx 2.847\ 10^{34} ergs\ s^{-1}$. This value should be bigger than the observed luminosities in the various bands. As an example the X-ray luminosity of PNs , L_X, in the wavelength band 5-28 Å has a range $[10^{30.9} \leftrightarrow 10^{31.2} ergs\ s^{-1}]$, see Table 3 in [64].

Due to the fact that is difficult to compute the volume in an asymmetric expansion the Sedov solution is adopted only in this paragraph.

3.3. Spherical Symmetry - Momentum Conservation

The thin layer approximation assumes that all the swept-up gas accumulates infinitely in a thin shell just after the shock front. The conservation of the radial momentum requires that

$$\frac{4}{3}\pi R^3 \rho \dot{R} = M_0 \quad , \tag{15}$$

where R and $\dot{R}$ are the radius and the velocity of the advancing shock , ρ the density of the ambient medium , M_0 the momentum evaluated at $t = t_0$, R_0 the initial radius and $\dot{R}_0$ the initial velocity , see [32, 65]. The law of motion is

$$R = R_0 \left(1 + 4 \frac{\dot{R}_0}{R_0}(t - t_0) \right)^{\frac{1}{4}} \quad . \tag{16}$$

and the velocity

$$\dot{R} = \dot{R}_0 \left(1 + 4 \frac{\dot{R}_0}{R_0}(t - t_0) \right)^{-\frac{3}{4}} \quad . \tag{17}$$

From equation (16) we can extract $\dot{R}_0$ and insert it in equation (17)

$$\dot{R} = \frac{1}{4(t - t_0)} \frac{R^4 - R_0^4}{R_0^3} \left(1 + \frac{R^4 - R_0^4}{R_0^4} \right)^{-\frac{3}{4}} \quad . \tag{18}$$

The astrophysical units are: t_4 and $t_{0,4}$ which are t and t_0 expressed in 10^4 yr units, R_{pc} and $R_{0,pc}$ which are R and R_0 expressed in pc, $\dot{R}_{kms}$ and $\dot{R}_{0,kms}$ which are $\dot{R}$ and $\dot{R}_0$ expressed in $\frac{km}{s}$. Therefore the previous formula becomes

$$\dot{R}_{kms} = 24.49 \frac{1}{(t_4 - t_{0,4})} \frac{R_{pc}^4 - R_{0,pc}^4}{R_{0,pc}^3} \left(1 + \frac{R_{pc}^4 - R_{0,pc}^4}{R_{0,pc}^4} \right)^{-\frac{3}{4}} \quad . \tag{19}$$

On introducing $R_{0,pc} = 0.1$, $R_{pc} = 0.78$, $\dot{R}_{kms} = 34.5 \frac{km}{s}$, the approximated age of A39 is found to be $t_4 - t_{0,4} = 50$ and $\dot{R}_{0,kms} = 181.2$.

3.4. Asymmetry - Exponential medium

Given the Cartesian coordinate system (x, y, z) , the plane $z = 0$ will be called equatorial plane and in polar coordinates $z = R\sin(\theta)$, where θ is the polar angle and R the distance from the origin . The presence of a non homogeneous medium in which the expansion takes place can be modeled assuming an exponential behavior for the number of particles of the type

$$n(z) = n_0 \exp{-\frac{z}{h}} = n_0 \exp{-\frac{R \times \sin(\theta)}{h}} \quad , \tag{20}$$

where R is the radius of the shell , n_0 is the number of particles at $R = R_0$ and h the scale. The 3D expansion will be characterized by the following properties

- Dependence of the momentary radius of the shell on the polar angle θ that has a range $[-90° \leftrightarrow +90°]$.

- Independence of the momentary radius of the shell from ϕ , the azimuthal angle in the x-y plane, that has a range $[0° \leftrightarrow 360°]$.

The mass swept, M, along the solid angle $\Delta\,\Omega$, between 0 and R is

$$M(R) = \frac{\Delta\,\Omega}{3} m_H n_0 I_m(R) + \frac{4}{3}\pi R_0^3 n_0 m_H \quad, \tag{21}$$

where

$$I_m(R) = \int_{R_0}^{R} r^2 \exp -\frac{r\sin(\theta)}{h} dr \quad, \tag{22}$$

where R_0 is the initial radius and m_H the mass of the hydrogen . The integral is

$$I_m(R) = \frac{h\left(2\,h^2 + 2\,R_0 h\sin\left(\theta\right) + R_0{}^2\left(\sin\left(\theta\right)\right)^2\right) e^{-\frac{R_0\sin(\theta)}{h}}}{\left(\sin\left(\theta\right)\right)^3}$$

$$-\frac{h\left(2\,h^2 + 2\,Rh\sin\left(\theta\right) + R^2\left(\sin\left(\theta\right)\right)^2\right) e^{-\frac{R\sin(\theta)}{h}}}{\left(\sin\left(\theta\right)\right)^3} \quad. \tag{23}$$

The conservation of the momentum gives

$$M(R)\dot{R} = M(R_0)\dot{R}_0 \quad, \tag{24}$$

where $\dot{R}$ is the velocity at R and $\dot{R}_0$ the initial velocity at $R = R_0$.

In this differential equation of the first order in R the variable can be separated and the integration term by term gives

$$\int_{R_0}^{R} M(r)dr = M(R_0)\dot{R}_0 \times (t - t_0) \quad, \tag{25}$$

where t is the time and t_0 the time at R_0. The resulting non linear equation $\mathcal{F}_{NL}$ expressed in astrophysical units is

$$\mathcal{F}_{NL} = -6\,e^{-\frac{R_{0,pc}\,\sin(\theta)}{h_{pc}}}\,h_{pc}{}^4 - h_{pc}\,e^{-\frac{R_{0,pc}\,\sin(\theta)}{h_{pc}}}\left(\sin\left(\theta\right)\right)^3 R_{0,pc}{}^3$$

$$-6\,h_{pc}{}^3 e^{-\frac{R_{0,pc}\,\sin(\theta)}{h_{pc}}}\sin\left(\theta\right) R_{0,pc} - 3\,h_{pc}{}^2 e^{-\frac{R_{0,pc}\,\sin(\theta)}{h_{pc}}}\left(\sin\left(\theta\right)\right)^2 R_{0,pc}{}^2$$

$$- R_{0,pc}{}^4\left(\sin\left(\theta\right)\right)^4 + 6\,e^{-\frac{R_{pc}\,\sin(\theta)}{h_{pc}}}\,h_{pc}{}^4 + 4\,e^{-\frac{R_{pc}\,\sin(\theta)}{h_{pc}}}\,h_{pc}{}^3 R_{pc}\,\sin\left(\theta\right)$$

$$+ e^{-\frac{R_{pc}\,\sin(\theta)}{h_{pc}}}\,h_{pc}{}^2 R_{pc}{}^2\left(\sin\left(\theta\right)\right)^2$$

$$+2\,e^{-\frac{R_{0,pc}\,\sin(\theta)}{h_{pc}}}\,h_{pc}{}^3 R_{pc}\,\sin\left(\theta\right) + 2\,e^{-\frac{R_{0,pc}\,\sin(\theta)}{h_{pc}}}\,h_{pc}{}^2 R_{pc}\left(\sin\left(\theta\right)\right)^2 R_{0,pc}$$

$$+ e^{-\frac{R_{0,pc}\,\sin(\theta)}{h_{pc}}}\,h_{pc}\,R_{pc}\left(\sin\left(\theta\right)\right)^3 R_{0,pc}{}^2$$

$$+ \left(\sin\left(\theta\right)\right)^4 R_{0,pc}{}^3 R_{pc} - 0.01\left(\sin\left(\theta\right)\right)^4 R_{0,pc}{}^3 \dot{R}_{0,kms}\,(t_4 - t_{0,4}) = 0 \quad, \tag{26}$$

where t_4 and $t_{0,4}$ are t and t_0 expressed in 10^4 yr units, R_{pc} and $R_{0,pc}$ are R and R_0 expressed in pc, $\dot{R}_{kms}$ and $\dot{R}_{0,kms}$ are $\dot{R}$ and $\dot{R}_0$ expressed in $\frac{km}{s}$, θ is expressed in radians and h_{pc} is the the scale , h , expressed in pc. It is not possible to find R_{pc} analytically and a numerical method should be implemented. In our case in order to find the root of $\mathcal{F}_{NL}$, the FORTRAN SUBROUTINE ZRIDDR from [66] has been used.

The unknown parameter $t_4 - t_{0,4}$ can be found from different runs of the code once $R_{0,pc}$ is fixed as $\approx 1/10$ of the observed equatorial radius , $\dot{R}_{0,kms}$ is 200 or less and $h_{pc} \approx 2 \times R_{0,pc}$.

3.5. Asymmetry - Power law medium

A possible form for a power law profile of the medium surrounding the Homunculus nebula is

$$n(z) = n_0 \left(\frac{z}{R_0}\right)^{-\alpha} \quad , \tag{27}$$

where $z = R \times \sin(\theta)$ is the distance from the equatorial plane, R is the instantaneous radius of expansion, n_0 is the number of particles at $R = R_0$, R_0 is the scale and α is a coefficient > 0.

The swept mass, M, along the solid angle $\Delta\,\Omega$ between 0 and R is

$$M(R) = \frac{\Delta\,\Omega}{3} 1.4\, m_H n_0 I_m(R) + \frac{4}{3}\pi R_0^3 n_0 m_H\, 1.4 \quad , \tag{28}$$

where

$$I_m(R) = \int_{R_0}^{R} r^2 \left(\frac{r\sin(\theta)}{R_0}\right)^{-\alpha} dr \quad , \tag{29}$$

where R_0 is the initial radius and m_H is the mass of hydrogen. The integral is

$$I_m(R) = \frac{R^3 \left(\frac{R\sin(\theta)}{R0}\right)^{-\alpha}}{3 - \alpha} \quad . \tag{30}$$

Conservation of momentum gives

$$M(R)\dot{R} = M(R_0)\dot{R}_0 \quad , \tag{31}$$

where $\dot{R}$ is the velocity at R and $\dot{R}_0$ is the initial velocity at $R = R_0$, $M(R)$ and $M(R_0)$ are the swept masses at R and R_0 respectively

In this first-order differential equation in R, the variables can be separated. Integration term-by-term gives

$$\int_{R_0}^{R} M(r)dr = M(R_0)\dot{R}_0 \times (t - t_0) \quad , \tag{32}$$

where t is the time and t_0 is the time at R_0. The resulting non-linear equation $\mathcal{F}_{NL}$ expressed in astrophysical units is

$$\begin{aligned}
\mathcal{F}_{NL} = &- R_{0,pc}{}^4 \alpha^2 + R_{pc}\, R_{0,pc}{}^3 \alpha^2 + R_{pc}\, R_{0,pc}{}^3 \left(\sin\left(\theta\right)\right)^{-\alpha} \alpha \\
&+ 7.0\, R_{0,pc}{}^4 \alpha - R_{0,pc}{}^4 \left(\sin\left(\theta\right)\right)^{-\alpha} \alpha - 7.0\, R_{pc}\, R_{0,pc}{}^3 \alpha \\
&+ 3\, R_{0,pc}{}^4 \left(\sin\left(\theta\right)\right)^{-\alpha} - 12\, R_{0,pc}{}^4 - 4.0\, R_{pc}\, R_{0,pc}{}^3 \left(\sin\left(\theta\right)\right)^{-\alpha} \\
&+ R_{pc}{}^{-\alpha+4.0} R_{0,pc}{}^\alpha \left(\sin\left(\theta\right)\right)^{-\alpha} + 12\, R_{pc}\, R_{0,pc}{}^3 \\
&-0.122\, R_{0,pc}{}^3 \dot{R}_{0,kms} \left(t_4 - t_{0,4}\right) - 0.01\, R_{0,pc}{}^3 \dot{R}_{0,kms} \left(t_4 - t_{0,4}\right) \alpha^2 \\
&+ 0.0714\, R_{0,pc}{}^3 \dot{R}_{0,kms} \left(t_4 - t_{0,4}\right) \alpha = 0 \quad , \tag{33}
\end{aligned}$$

where t_4 and $t_{0,4}$ are t and t_0 expressed in 10^4 yr units, R_{pc} and $R_{0,pc}$ are R and R_0 expressed in pc, $\dot{R}_{kms}$ and $\dot{R}_{0,kms}$ are $\dot{R}$ and $\dot{R}_0$ expressed in $\frac{km}{s}$ and θ is expressed in radians.

It is not possible to find R_{pc} analytically and a numerical method must be implemented. In our case, in order to find the root of $\mathcal{F}_{NL}$, the FORTRAN SUBROUTINE ZRIDDR from [66] has been used. The unknown parameters, $R_{0,pc}$ and $\dot{R}_{0,kms}$, are found from different runs of the code, $t_4 - t_{0,4}$ is an input parameter.

Table 1. Data of the simulation of the PN Ring nebula

Initial expansion velocity ,$\dot{R}_{0,kms}$	200
Age $(t_4 - t_{0,4})$	0.12
Initial radius $R_{0,pc}$	0.035
scaling h_{pc}	$2 \times R_{0,pc}$

4.   Applications of the law of motion

From a practical point of view, ϵ , the percentage of reliability of our code can also be introduced,

$$\epsilon = (1 - \frac{|(R_{\mathrm{pc,obs}} - R_{pc,\mathrm{num}})|}{R_{pc,\mathrm{obs}}}) \cdot 100 \,, \tag{34}$$

where $R_{pc,\mathrm{obs}}$ is the radius as given by the astronomical observations in parsec , and $R_{pc,\mathrm{num}}$ the radius obtained from our simulation in parsec.

In order to test the simulation over different angles, an observational percentage of reliability ,ϵ_{obs}, is introduced which uses both the size and the shape,

$$\epsilon_{\mathrm{obs}} = 100(1 - \frac{\sum_j |R_{pc,\mathrm{obs}} - R_{pc,\mathrm{num}}|_j}{\sum_j R_{pc,\mathrm{obs},j}}), \tag{35}$$

where the index j varies from 1 to the number of available observations.

4.1.   Simulation of a PN , Ring nebula

A typical set of parameters that allows us to simulate the Ring nebula is reported in Table 1.

The complex 3D behavior of the advancing Ring nebula is reported in Figure 3 and Figure 4 reports the asymmetric expansion in a section crossing the center. In order to better visualize the asymmetries Figure 5 and Figure 6 report the radius and the velocity as a function of the position angle θ. The combined effect of spatial asymmetry and field of velocity are reported in Figure 7.

The efficiency of our code in reproducing the observed radii as given by formula (34) and the efficiency when the age is five time greater are reported in Table 2.

An analogous formula allows us to compute the efficiency in the computation of the maximum velocity , see Table 3.

4.2.   Simulation of PN , MyCn 18

A typical set of parameters that allows us to simulate MyCn 18 is reported in Table 4.

The bipolar behavior of the advancing MyCn 18 is reported in Figure 8 and Figure 9 reports the expansion in a section crossing the center. It is interesting to point out the similarities between our Figure 9 of MyCn 18 and Figure 1 in [16] which define the parameters a and h of the Atlas of synthetic line profiles. In order to better visualize the two lobes Figure 10 reports the radius as a function of the position angle θ.
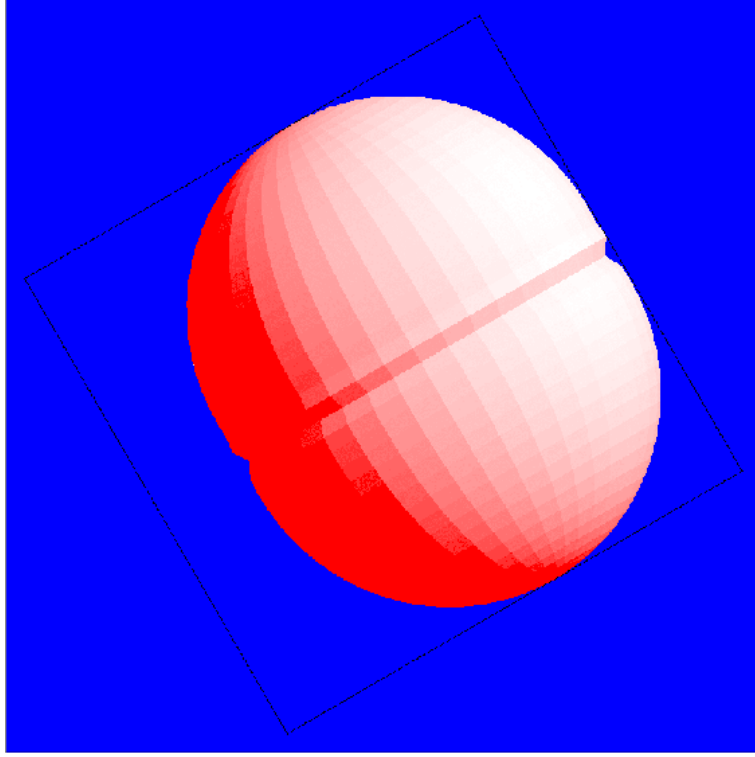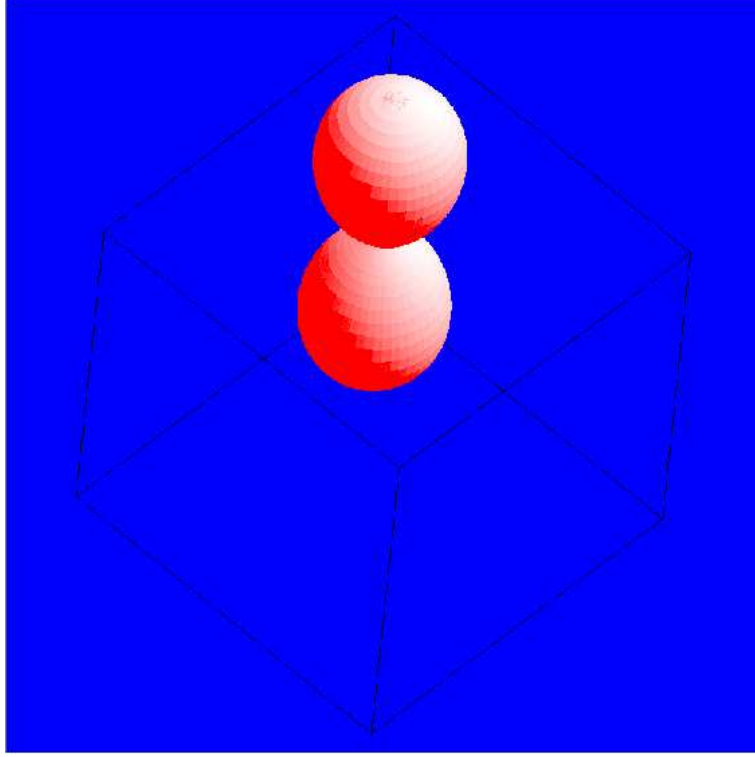
Figure 3. Continuous three-dimensional surface of the PN Ring nebula : the three Eulerian angles characterizing the point of view are Φ=180 °, Θ=90 ° and Ψ=-30 °. Physical parameters as in Table 1.

Table 2. Reliability of the radii of the PN Ring nebula.

	$R_{\mathrm{up}}(\mathrm{pc})$ *polar direction*	$R_{\mathrm{eq}}(\mathrm{pc})$ *equatorial plane*
R_{obs}	0.14	0.1
R_{num}(our code)	0.125	0.102
$\epsilon(\%)$	89	97
ϵ (%) *for a time* 5 *times greater*	27	41
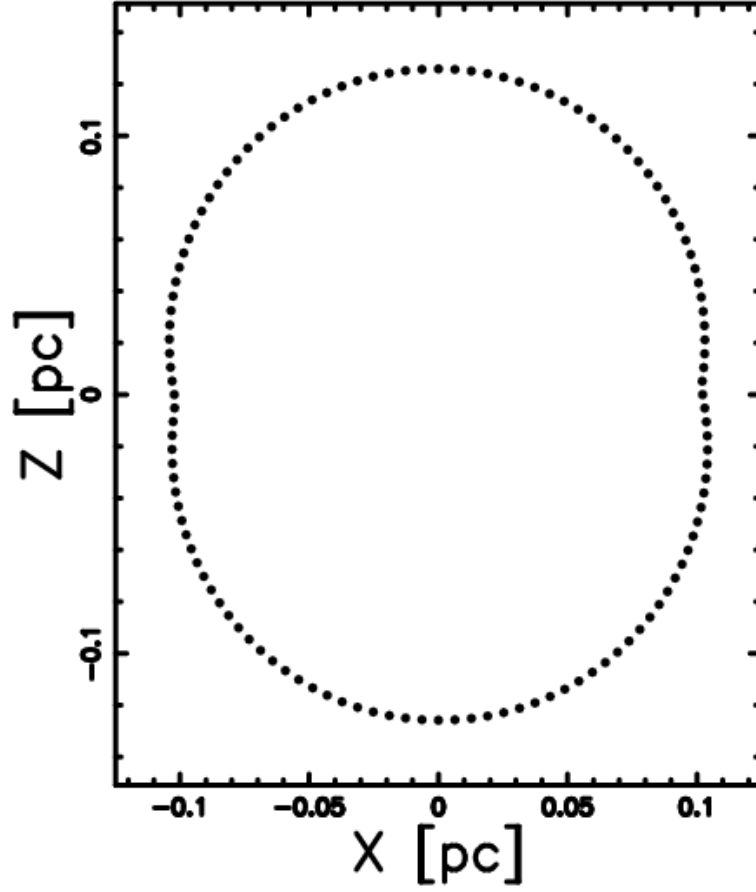
Figure 4. Section of the PN Ring nebula on the *x-z* plane. The horizontal and vertical axis are in *pc*. Physical parameters as in Table 1.

Table 3. Reliability of the velocity of the PN Ring nebula

	$V(\frac{km}{s})$ *maximum velocity*
V_{obs}	48.79
V_{num}	39.43
$\epsilon(\%)$	80.81
$\epsilon(\%)$ (%) *for a time* 5 *times greater*	35.67
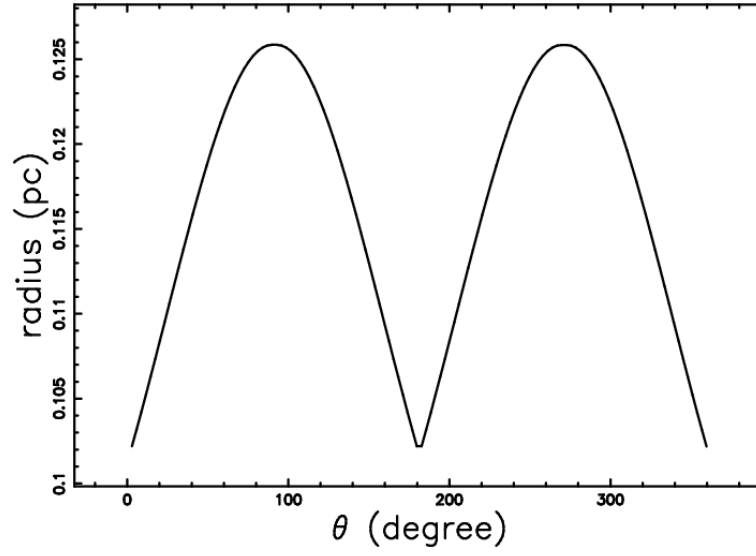
Figure 5.   Radius in pc of the PN Ring nebula as a function of the position angle in degrees. Physical parameters as in Table 1.
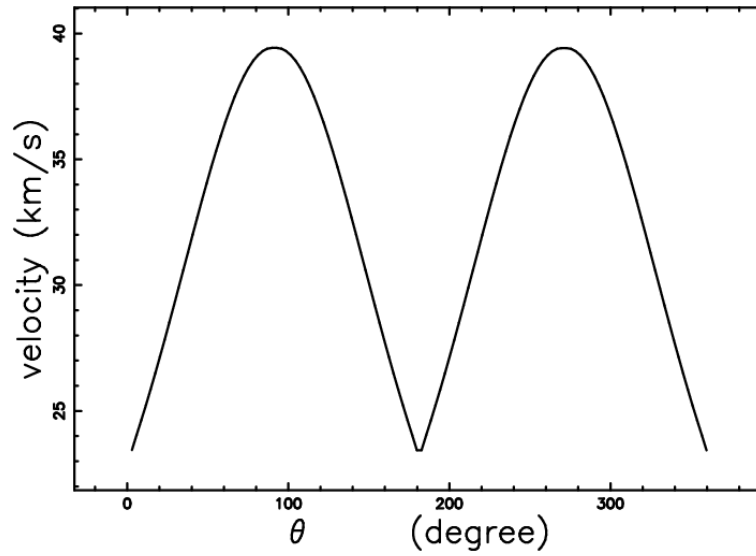
Figure 6.   Velocity in $\frac{km}{s}$ of the PN Ring nebula as a function of the position angle in degrees. Physical parameters as in Table 1.
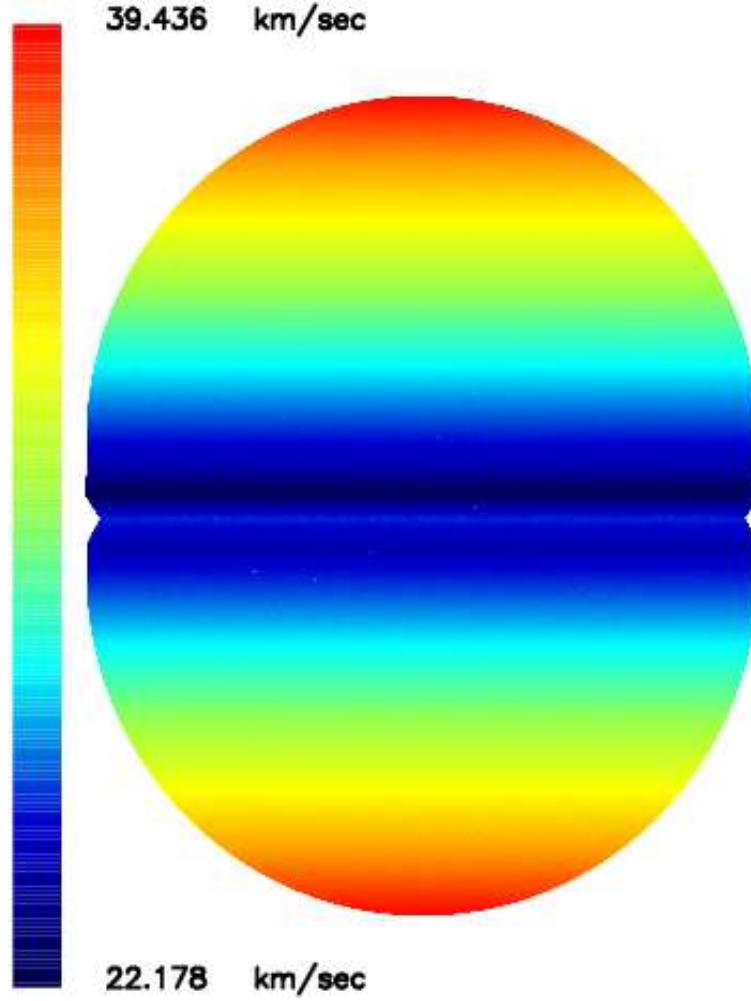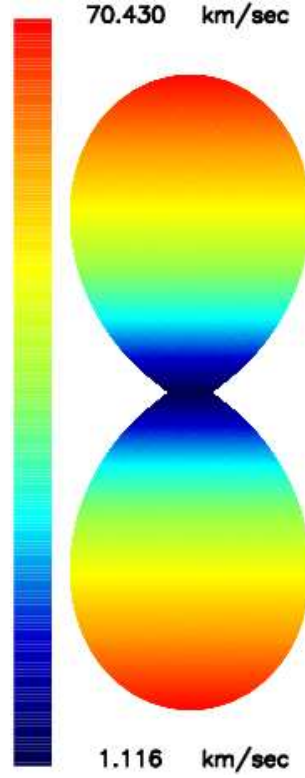
Figure 7.   Map of the expansion velocity in $\frac{km}{s}$ relative to the simulation of the PN Ring nebula when 300000 random points are selected on the surface. Physical parameters as in Table 1.

Table 4. Data of the simulation of the PN MyCn 18

Initial expansion velocity ,$\dot{R}_{0,kms}$ [km s^{-1}]	200
Age $(t_4 - t_{0,4})$ [10^4 yr]	0.2
Initial radius $R_{0,pc}$ [pc]	0.001
scaling h [pc]	$1.0 \times R_0$

Figure 8.   Continuous three-dimensional surface of the PN MyCn 18 : the three Eulerian angles characterizing the point of view are Φ=130 °, Θ=40 ° and Ψ=5 °. Physical parameters as in Table 4.
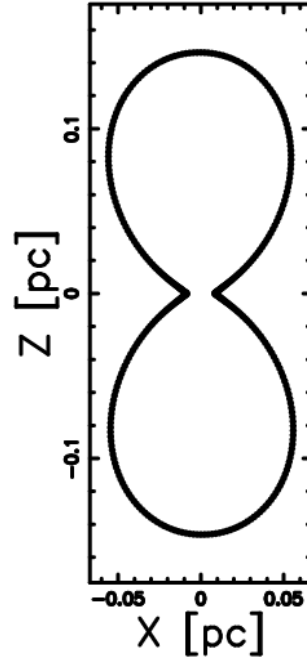
Figure 9. Section of the PN MyCn 18 on the *x-z* plane. Physical parameters as in Table 4.
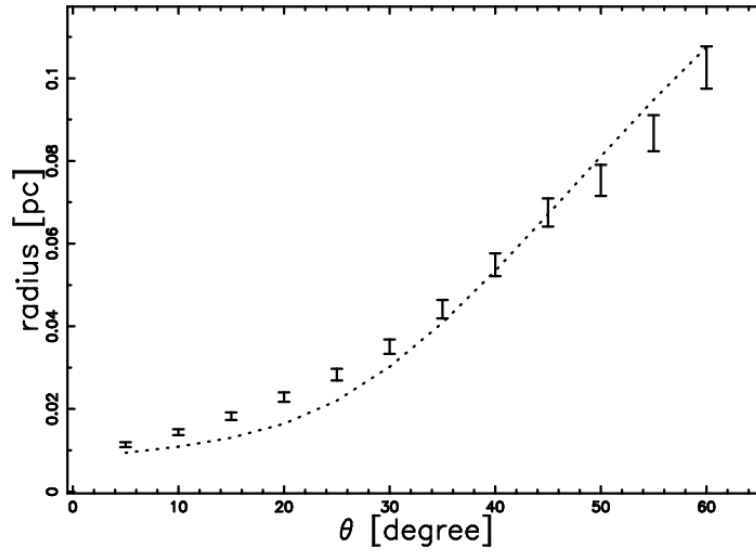
Figure 10. Radius in pc of the PN MyCn 18 as a function of latitude from 0° to 60° (dotted line) when the physical parameters are those of Table 4. The points with error bar (1/10 of the value) represent the data of Table 1 in Dayal et al. 2000.

Figure 11.   Map of the expansion velocity in $\frac{km}{s}$ relative to the simulation of the PN MyCn 18 when 300000 random points are selected on the surface. Physical parameters as in Table 4.

The combined effect of spatial asymmetry and field of velocity are reported in Figure 11.

The efficiency of our code in reproducing the spatial shape over 12 directions of MyCn 18 as given by formula (35) is reported in Table 5. This Table also reports the efficiency in simulating the shape of the velocity.

Figure   12 reports our results as well those of Table 1 in [46].

4.3.   Simulation of η-Carinae in an exponentially varying medium

A typical set of parameters which allows the Homunculus nebula around η-Carinae to be simulated in the presence of a medium whose density decreases exponentially is reported

Table 5. Reliability of the spatial and velocity shape of the PN MyCn 18.

	radius	velocity
$\epsilon_{obs}(\%)$	90.66	57.68
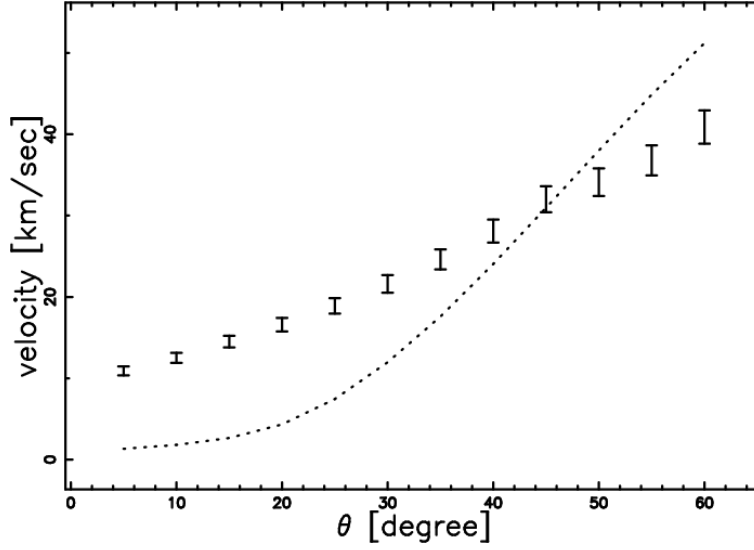
Figure 12. Velocity in $\frac{km}{s}$ of the PN MyCn 18 as a function of the latitude in degrees when the physical parameters are those of Table 4, dotted line. The points with error bar (1/10 of the value) represent the data of Table 1 in Dayal et al. 2000.

in Table 6. Table 7 presents numbers concerning the quality of fit.

The bipolar character of the Homunculus is shown in Figure 13. In order to better visualize the two lobes, Figure 14 and Figure 15 show the radius and velocity as a function of the angular position θ. The orientation of the observer is characterized by the three Euler angles (Φ, Θ, Ψ), see [67]; different Euler angles produce different observed shapes.

The velocity field is shown in Figure 16.

The accuracy with which our code reproduces the spatial shape and the velocity field over 18 directions of the Homunculus nebula as given by formula (35) is reported in Table 7. From a careful analysis of Table 7 we can conclude that the spatial shape over 18 directions is well modeled by an exponential medium , $\epsilon_{obs} = 85\%$. The overall efficiency of the field is smaller $\epsilon_{obs} = 75\%$. We can therefore conclude that formula (35) which gives the efficiency over all the range of polar angles represents a better way to describe the results in respect to the efficiency in a single direction as given by formula (34).

4.4.   Simulation of η-Carinae for a power law medium

For assumed parameters see Table 6, Table 8 reports the accuracy of radius and velocity in two directions.

4.5.   Simulation of a spherical SNR , SN 1993J

According to the power solution as given by (4) and to the data used in Section 3.1., ϵ=98.54 %.

Table 6. Parameter values used to simulate the observations of the hybrid Homunculus/η-Carinae nebula for a medium varying exponentially (first 4 values) or a power law (2nd set of 4 values)

Initial expansion velocity, $\dot{R}_{0,1}$ [km s^{-1}]	8000
Age $(t_4 - t_{0,4})$ [10^4 yr]	0.0158
Scaling h [pc]	0.0018
Initial radius R_0 [pc]	0.001
Initial expansion velocity, $\dot{R}_{0,1}$ [km s^{-1}]	40,000
Age $(t_4 - t_{0,4})$ [10^4 yr]	0.0158
Initial radius R_0 [pc]	0.0002
Power law coefficient α	2.4

Table 7. Agreement between observations and simulations of the hybrid Homunculus/η-Carinae nebula, for an exponentially varying medium.

	radius	velocity
$\epsilon(\%) - polar\ direction$	97	99
$\epsilon(\%) - equatorial\ direction$	87	19
$\epsilon_{obs}(\%)$	85	75

Table 8. Agreement between model for a power law medium and observations for the hybrid Homunculus/η-Carinae nebula.

	radius	velocity
$\epsilon(\%) - polar\ direction$	78	76
$\epsilon(\%) - equatorial\ direction$	6	2
$\epsilon_{obs}(\%)$	79	73
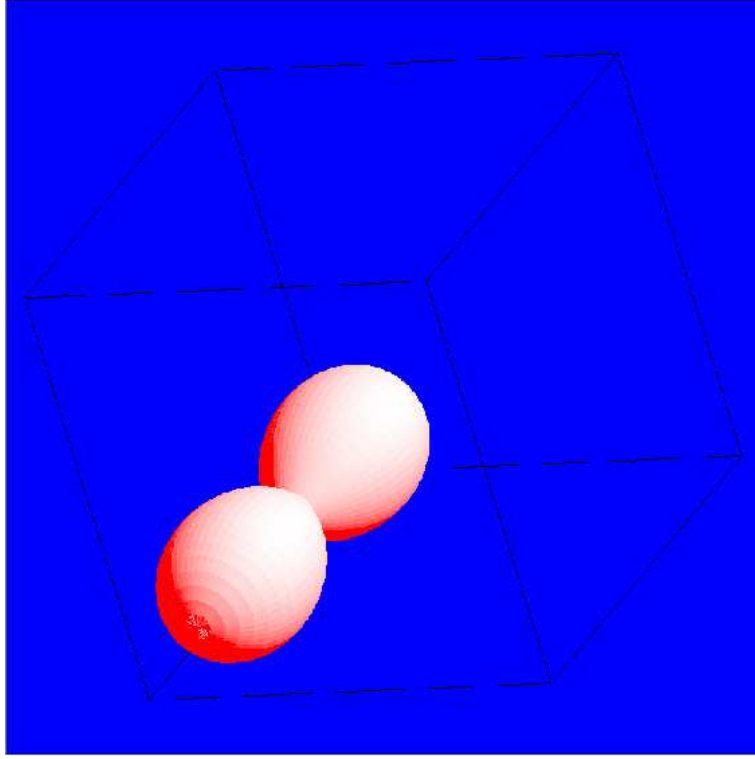
Figure 13.   Simulations lead to this picture of the hybrid Homunculus/η-Carinae nebula for an exponentially varying medium. The orientation of the figure is characterized by the Euler angles , which are Φ=130°, Θ=40° and Ψ=-140°. Physical parameters as in Table 6.
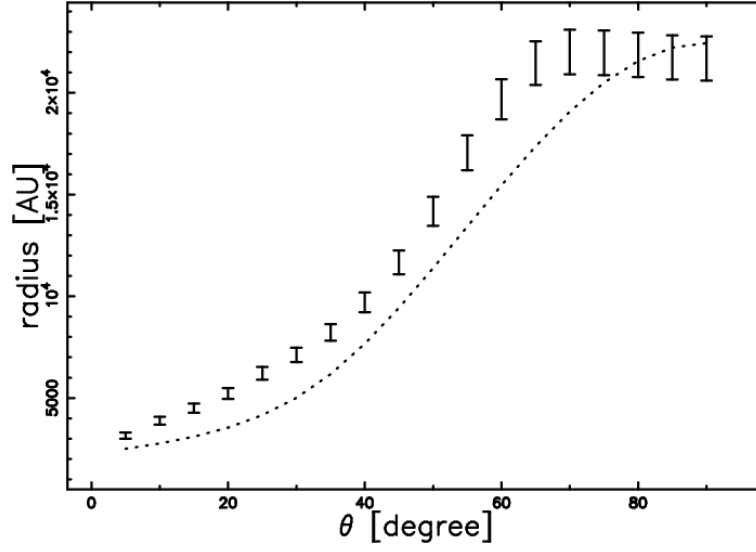
Figure 14. Radius of the hybrid Homunculus/η-Carinae nebula as a function of latitude for an exponentially varying medium (dotted line) and astronomical data with error bar. Physical parameters as in Table 6.
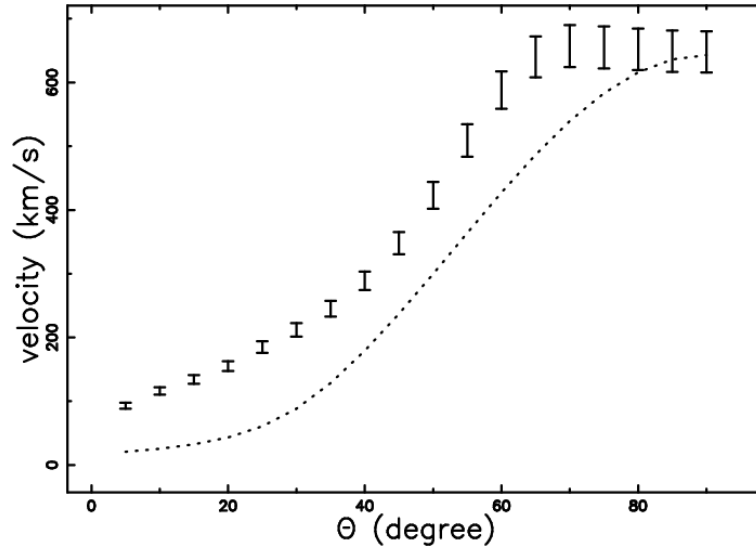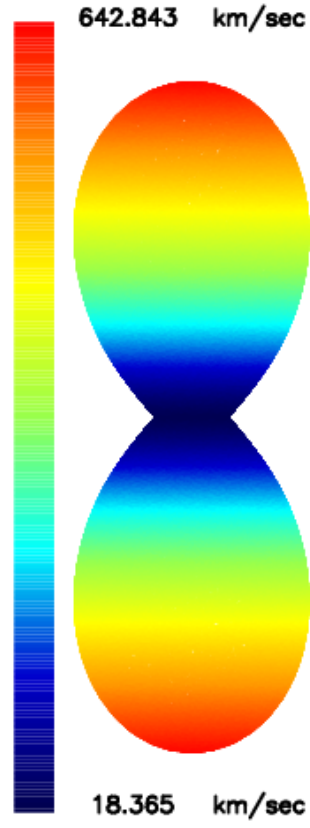

Figure 15. Velocity of the hybrid Homunculus/η-Carinae nebula as a function of latitude for an exponentially varying medium (dotted line) and astronomical data with error bar Physical parameters as in Table 6.

Figure 16. Map of the expansion velocity for an exponentially varying medium relative to the hybrid Homunculus/η-Carinae nebula. Physical parameters as in Table 6.
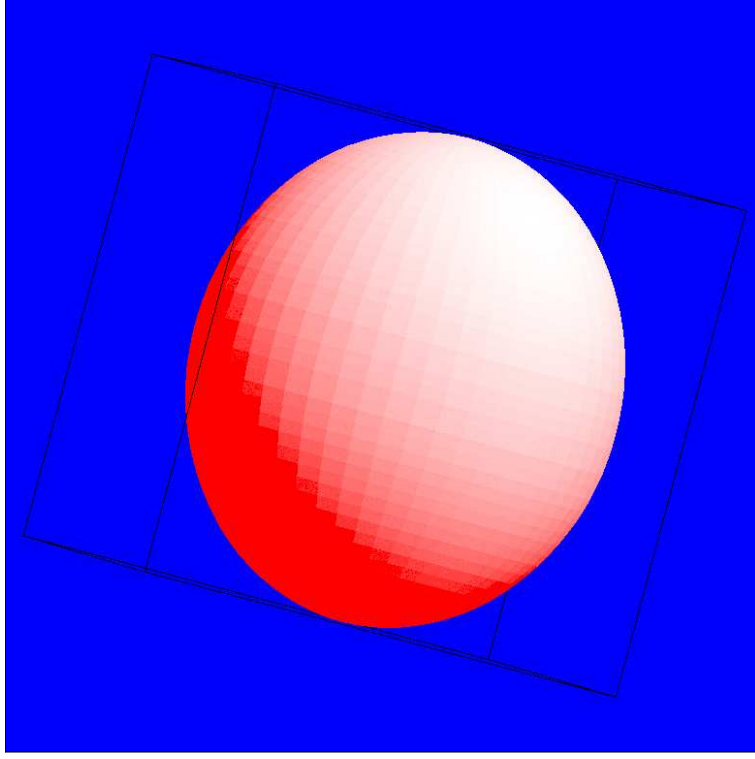
Figure 17. The shape of the expanding envelope modeled by 2500 faces particularized for SN 1006 . The three Eulerian angles characterizing the point of view are Φ=75 $^\circ$, Θ=90 $^\circ$ and Ψ=75 $^\circ$.

4.6.   Simulation of a asymmetric SNR , SN 1006

According to the numerical code developed in [68] in the case of a Gaussian profile we have $\epsilon = 94.9\%$ in the polar direction and $\epsilon = 92.5\%$ in the equatorial direction. From a practical point of view, the range of the polar angle θ (180°) is divided into n_θ steps and the range of the azimuthal angle ϕ (360°) into n_ϕ steps. This yields $(n_\theta + 1)\,(n_\phi + 1)$ directions of motion which can also be identified with the number of vertexes of the polyhedron representing the volume occupied by the explosion ; this polyhedron varies from a sphere to an irregular shape on the basis of the swept–up material in each direction . In the plots showing the expansion surface of the explosion, the number of vertexes $(n_\theta + 1)\cdot(n_\phi + 1)$ and the number of the faces $n_\theta \cdot\ n_\phi$; are specified, for example in Figure 17 n_θ=50 and n_ϕ=50.

5.   Diffusion

The mathematical diffusion allows us to follow the number density of particles from high values (injection) to low values (absorption). We recall that the number density is expressed in $\frac{particles}{unit\ volume}$ and the symbol C is used in the mathematical diffusion and the symbol n in an astrophysical context. The density ρ is obtained by multiplying n by the mass of hydrogen

, m_H , and by a multiplicative factor , f, which varies from 1.27 in [69] to 1.4 in [33]

$$\rho = f m_H n \quad . \tag{36}$$

The physical process that allows the particles to diffuse is hidden in the mathematical diffusion. In our case the physical process can be the random walk with a time step equal to the Larmor gyroradius. In the Monte Carlo diffusion the step-length of the random walk is generally taken as a fraction of the side of the considered box. Both mathematical diffusion and Monte Carlo diffusion use the concept of absorbing-boundary which is the spatial coordinate where the diffusion path terminates.

In the following, 3D mathematical diffusion from a sphere and 1D mathematical as well Monte Carlo diffusion in presence of drift and are considered.

5.1.   3D diffusion from a spherical source

Once the number density , C, and the diffusion coefficient ,D, are introduced , Fick' s first equation changes expression on the basis of the adopted environment , see for example equation (2.5) in [70]. In three dimensions it is

$$\frac{\partial C}{\partial t} = D \nabla^2 C \quad , \tag{37}$$

where t is the time and ∇^2 is the Laplacian differential operator.

In presence of the steady state condition:

$$D \nabla^2 C = 0 \quad . \tag{38}$$

The number density rises from 0 at $r=a$ to a maximum value C_m at $r=b$ and then falls again to 0 at $r=c$. The solution to equation (38) is

$$C(r) = A + \frac{B}{r} \quad , \tag{39}$$

where A and B are determined by the boundary conditions ,

$$C_{ab}(r) = C_m \left(1 - \frac{a}{r}\right) \left(1 - \frac{a}{b}\right)^{-1} \quad a \leq r \leq b \quad , \tag{40}$$

and

$$C_{bc}(r) = C_m \left(\frac{c}{r} - 1\right) \left(\frac{c}{b} - 1\right)^{-1} \quad b \leq r \leq c \quad . \tag{41}$$

These solutions can be found in [70] or in [71] .

5.2.   1D diffusion with drift, mathematical diffusion

In one dimension and in the presence of a drift velocity ,u, along the radial direction the diffusion is governed by Fick's second equation , see equation (4.5) in [70] ,

$$\frac{\partial C}{\partial t} = D \frac{\partial^2 C}{\partial r^2} - \vec{u} \frac{\partial C}{\partial r} \quad , \tag{42}$$
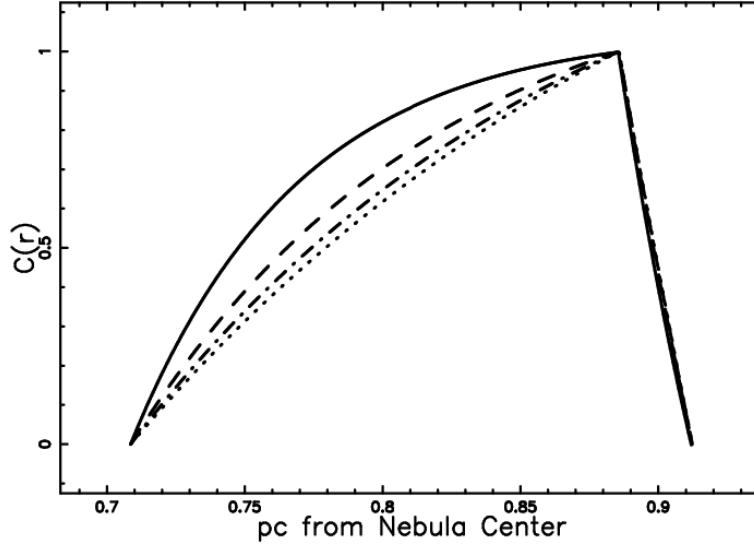
Figure 18. Number density of the PN A39 as a function of the distance in pc from the injection when $u = 1$, $C_m = 1$, $a = 69.6 \; arcsec$, $b = 87 \; arcsec$, $c = 89.6 \; arcsec$ and $D = 2$ (full line), $D = 7$ (dashed), $D = 12$ (dot-dash-dot-dash) and $D = 17$ (dotted). The conversion from $arcsec$ to pc is done assuming a distance of $2100 \; pc$ for A39.

where $\vec{u}$ can take two directions. The number density rises from 0 at *r=a* to a maximum value C_m at *r=b* and then falls again to 0 at *r=c* . The general solution to equation (42) in presence of a steady state is

$$C(r) = A + B e^{\frac{\vec{u}}{D} r} \quad . \tag{43}$$

We now assume that *u* and *r* do not have the same direction and therefore *u* is negative ; the solution is

$$C(r) = A + B e^{-\frac{u}{D} r} \quad , \tag{44}$$

and now the velocity *u* is a scalar.

The boundary-conditions give

$$C_{a,b,drift}(r) = C_m \frac{e^{-\frac{u}{D} a} - e^{-\frac{u}{D} r}}{e^{-\frac{u}{D} a} - e^{-\frac{u}{D} b}} \quad a \le r \le b \quad downstream \; side \quad , \tag{45}$$

and

$$C_{b,c,drift}(r) = C_m \frac{e^{-\frac{u}{D} c} - e^{-\frac{u}{D} r}}{e^{-\frac{u}{D} c} - e^{-\frac{u}{D} b}} \quad b \le r \le c \quad upstream \; side \quad . \tag{46}$$

A typical plot of the number density for different values of the diffusion coefficient is reported in Figure 18.

5.3. 1D diffusion with drift, random walk

Given a 1D segment of length *side* we can implement the random walk with step-length λ by introducing the numerical parameter $NDIM = \frac{side}{\lambda}$. We now report the adopted rules when the injection is in the middle of the grid :

1. The first of the $NPART$ particles is chosen.

2. The random walk of a particle starts in the middle of the grid. The probabilities of having one step are p_1 in the negative direction (downstream) , $p_1 = \frac{1}{2} - \mu \times \frac{1}{2}$, and p_2 in the positive direction (upstream) , $p_2 = \frac{1}{2} + \mu \times \frac{1}{2}$, where μ is a parameter that characterizes the asymmetry ($0 \leq \mu \leq 1$).

3. When the particle reaches one of the two absorbing points , the motion starts another time from (ii) with a different diffusing pattern.

4. The number of visits is recorded on $\mathcal{M}$, a one–dimensional grid.

5. The random walk terminates when all the $NPART$ particles are processed.

6. For the sake of normalization the one–dimensional visitation or number density grid $\mathcal{M}$ is divided by $NPART$.

There is a systematic change of the average particle position along the x-direction:

$$\langle dx \rangle = \mu \, \lambda \quad , \tag{47}$$

for each time step. If the time step is $dt = \frac{\lambda}{v_{tr}}$ where v_{tr} is the transport velocity, the asymmetry ,μ , that characterizes the random walk is

$$\mu = \frac{u}{v_{tr}} \quad . \tag{48}$$

Figure 19 reports $\mathcal{M}(x)$, the number of visits generated by the Monte Carlo simulation as well as the mathematical solution represented by formulas (45) and (46).

The solutions of the mathematical diffusion equations (45) and (46) can be rewritten at the light of the random walk and are

$$C_{a,b,MC}(r) = C_m \frac{e^{-\frac{2\mu}{\lambda}a} - e^{-\frac{2\mu}{\lambda}r}}{e^{-\frac{2\mu}{\lambda}a} - e^{-\frac{2\mu}{\lambda}b}} \quad a \leq r \leq b \quad downstream\ side \quad , \tag{49}$$

and

$$C_{b,c,MC}(r) = C_m \frac{e^{-\frac{2\mu}{\lambda}c} - e^{-\frac{2\mu}{\lambda}r}}{e^{-\frac{2\mu}{\lambda}c} - e^{-\frac{2\mu}{\lambda}b}} \quad b \leq r \leq c \quad upstream\ side \quad . \tag{50}$$

6.   Radiative transfer equation

The transfer equation in the presence of emission only , see for example [72] or [73] , is

$$\frac{dI_\nu}{ds} = -k_\nu \zeta I_\nu + j_\nu \zeta \quad , \tag{51}$$

where I_ν is the specific intensity , s is the line of sight , j_ν the emission coefficient, k_ν a mass absorption coefficient, ζ the mass density at position s and the index ν denotes the interested frequency of emission. The solution to equation (51) is

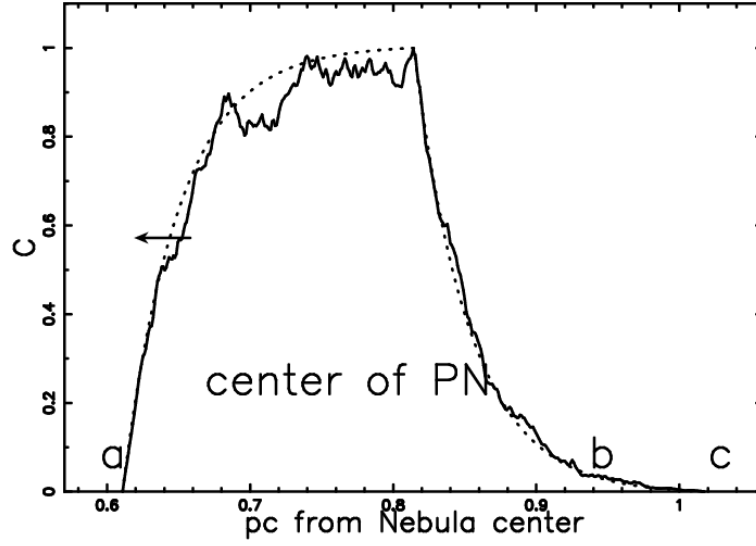$$I_\nu(\tau_\nu) = \frac{j_\nu}{k_\nu}(1 - e^{-\tau_\nu(s)}) \quad , \tag{52}$$

Figure 19.   Number density relative to PN A39 of the 1D asymmetric random walk (full line), NDIM=401 ,NPART=200 ,$side = 40\ arcsec$, $\lambda = 0.1\ arcsec$ and μ =- 0.013. For astrophysical purposes μ is negative. The theoretical number density as represented by formulas (45) and (46) is reported when $u = 1$, $C_m = 1$, $a = 60\ arcsec$, $b = 80\ arcsec$, $c = 100\ arcsec$ and $D = 3.84$ (dotted line). The conversion from $arcsec$ to pc is done assuming a distance of 2100 pc for A39.

where τ_ν is the optical depth at frequency ν

$$d\tau_\nu = k_\nu \zeta ds \quad . \tag{53}$$

We now continue analyzing the case of an optically thin layer in which τ_ν is very small (or k_ν very small) and the density ζ is substituted with our number density C(s) of particles. Two cases are taken into account : the emissivity is proportional to the number density and the emissivity is proportional to the square of the number density . In the linear case

$$j_\nu \zeta = KC(s) \quad , \tag{54}$$

where K is a constant function. This can be the case of synchrotron radiation in presence of a isotropic distribution of electrons with a power law distribution in energy, $N(E)$,

$$N(E)dE = K_s E^{-\gamma_f} \quad , \tag{55}$$

where K_s is a constant. In this case the emissivity is

$$j_\nu \rho \approx 0.933 \times 10^{-23} \alpha(\gamma_f) K_s H_\perp^{\frac{\gamma_f+1}{2}} \Big(\frac{6.26 \times 10^{18}}{\nu}\Big)^{\frac{\gamma_f-1}{2}} \frac{erg}{s\,cm^3\,Hz\,rad^2}, \tag{56}$$

where ν is the frequency and $\alpha(\gamma_f)$ is a slowly varying function of γ_f which is of the order of unity and is given by

$$\alpha(\gamma_f) = 2^{(\gamma_f-3)/2} \frac{\gamma_f + 7/3}{\gamma_f + 1} \Gamma\Big(\frac{3\gamma_f - 1}{12}\Big) \Gamma\Big(\frac{3\gamma_f + 7}{12}\Big) \quad , \tag{57}$$

for $\gamma_f \geq \frac{1}{2}$, see formula (1.175) in [74] . The synchrotron emission is widely used to explain the radiation observed in SNR, see [75–80]. This non thermal radiation continuum emission was also detected in a PN associated with a very long-period OH/IR variable star (V1018 Sco), see [81].

   In the quadratic case

$$j_\nu \zeta = K_2 C(s)^2 \quad , \tag{58}$$

where K_2 is a constant function. This is true for

- Free-free radiation from a thermal plasma, see formula (1.219) in [74] . This radiation process was adopted by [48] in the little Homunculus.

- Thermal bremsstrahlung and recombination radiation , see formula (1.237) in [74] . This radiation process was adopted in PNs by [82–84].

The intensity is now

$$I_\nu(s) = K \int_{s_0}^s C(s\prime)ds\prime \quad \text{optically thin layer} \quad linear\ case \quad , \tag{59}$$

or

$$I_\nu(s) = K_2 \int_{s_0}^s C(s\prime)^2 ds\prime \quad \text{optically thin layer} \quad quadratic\ case \quad . \tag{60}$$

In the Monte Carlo experiments the number density is memorized on the grid $\mathcal{M}$ and the intensity is

$$I(i,j) = \sum_k \triangle s \times \mathcal{M}(i,j,k) \quad \text{optically thin layer} \quad \textit{linear case} \quad , \qquad (61)$$

or

$$I(i,j) = \sum_k \triangle s \times \mathcal{M}(i,j,k)^2 \quad \text{optically thin layer} \quad \textit{quadratic case} \quad , \qquad (62)$$

where $\triangle$s is the spatial interval between the various values and the sum is performed over the interval of existence of the index k. The theoretical intensity is then obtained by integrating the intensity at a given frequency over the solid angle of the source.

In order to deal with the transition to the optically thick case, the intensity is given by

$$I(i,j) = \frac{1}{K_a}(1 - \exp(-K_a \sum_k \triangle s \times \mathcal{S}(i,j,k))) \qquad (63)$$

$$\text{Thin} \longmapsto \text{Thick} \quad ,$$

where K_a is a constant that represents the absorption. Considering the Taylor expansion of the last formula (63), equation (61) is obtained.

7.   Images

The image of a PN , η-Carinae and a SNR can be modeled once an analytical or numerical law for the intensity of emission as a function of the radial distance from the center is given. Simple analytical results for the radial intensity can be deduced in the rim model when the length of the layer and the number density are constants. The integration of the solutions to the mathematical diffusion along the line of sight allows us to deduce analytical formulas in the spherical case. The complexity of the intensity in the aspherical case can be attached only from a numerical point of view.

7.1.   3D Constant Number density in a rim model

We assume that the number density C is constant and in particular rises from 0 at $r = a$ to a maximum value C_m , remains constant up to $r = b$ and then falls again to 0. This geometrical description is reported in Figure 20. The length of sight , when the observer is situated at the infinity of the x-axis , is the locus parallel to the x-axis which crosses the position y in a Cartesian $x - y$ plane and terminates at the external circle of radius b. The locus length is

$$l_{0a} = 2 \times (\sqrt{b^2 - y^2} - \sqrt{a^2 - y^2}) \quad ; 0 \le y < a$$
$$l_{ab} = 2 \times (\sqrt{b^2 - y^2}) \quad ; a \le y < b \quad . \qquad (64)$$

When the number density C_m is constant between two spheres of radius a and b the intensity of radiation is

$$I_{0a} = C_m \times 2 \times (\sqrt{b^2 - y^2} - \sqrt{a^2 - y^2}) \quad ; 0 \le y < a$$
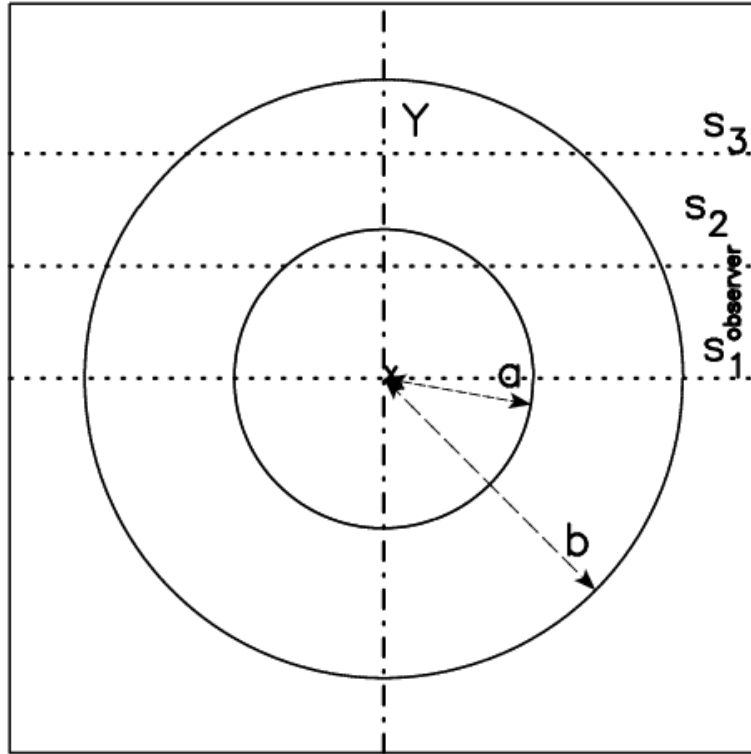$$I_{ab} = C_m \times 2 \times (\sqrt{b^2 - y^2}) \quad ; a \le y < b \quad . \qquad (65)$$

Figure 20.   The two circles (section of spheres) which include the region with constant density are represented through a full line. The observer is situated along the x direction, and three lines of sight are indicated.
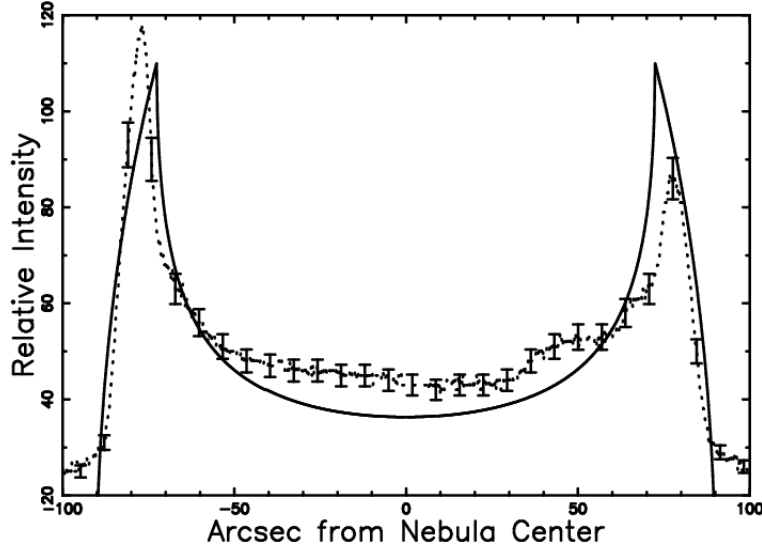
Figure 21. Cut of the mathematical intensity I of the rim model (equation (65)) crossing the center (full line) of the PN A39 and real data (dotted line with some error bar) . The number of data is 801 and for this model $\chi^2 = 1.487$ against $\chi^2 = 0.862$ of the rim model fully described in Jacoby et al. (2001).

The comparison of observed data of A39 and the theoretical intensity is reported in Figure 21 when data from Table 9 are used.

The ratio between the theoretical intensity at the maximum , $(y = b)$, and at the minimum , $(y = 0)$, is given by

$$\frac{I(y = b)}{I(y = 0)} = \frac{\sqrt{b^2 - a^2}}{b - a} \quad . \tag{66}$$

7.2.   3D diffusion from a sphere, square dependence

Figure 22 shows a spherical shell source of radius b between a spherical absorber of radius a and a spherical absorber of radius c.

The number density rises from 0 at $r=a$ to a maximum value C_m at $r=b$ and then falls again to 0 at $r=c$.

The numbers density to be used are formulas (40) and (41) once $r = \sqrt{x^2 + y^2}$ is imposed ; these two numbers density are inserted in formula (58) which represents the transfer equation with a quadratic dependence on the number density. An analogous case was solved in [85] by adopting a linear dependence on the number density . The geometry of the phenomena fixes three different zones $(0 - a, a - b, b - c)$ in the variable y, ; the first

Table 9. Simulation of the PN A39 with the rim model

symbol	meaning	value
a	radius of the internal sphere	$72.5''$
b	radius of the external sphere	$90.18''$
R_{shell}	observed radius of the shell	$77''$
$\delta r_{shell,t}$	theoretical thickness of the shell	$17.6''$
δr_{shell}	observed thickness of the shell	$10.1''$
$\frac{I_{limb}}{I_{center}}$	ratio of observed intensities	$(1.88 - 2.62)$
$\frac{I_{max}}{I(y=0)}$	ratio of theoretical intensities	3.03
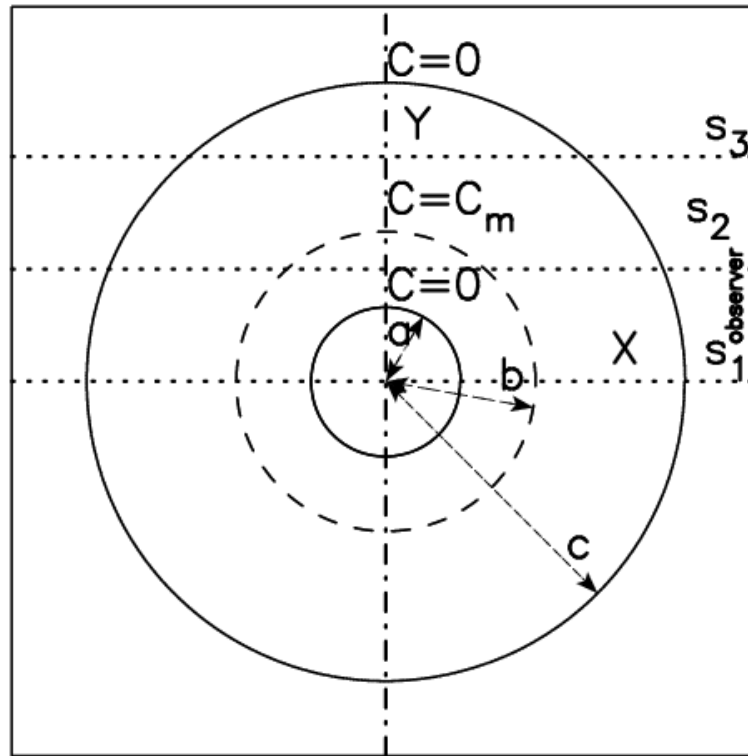
Figure 22.   The spherical source inserted in the great box is represented through a dashed line, and the two absorbing boundaries with a full line. The observer is situated along the x direction, and three lines of sight are indicated. Adapted from Figure 3.1 by Berg (1993) .

piece , $I^I(y)$, is

$$I^I(y) = \int_{\sqrt{a^2-y^2}}^{\sqrt{b^2-y^2}} 2C_{ab}^2 dx + \int_{\sqrt{b^2-y^2}}^{\sqrt{c^2-y^2}} 2C_{bc}^2 dx$$

$$= -2\frac{C_m{}^2 b^2}{y(b^2 - 2\,ba + a^2)(c^2 - 2\,cb + b^2)}\Big[-2\,a^2\arctan(\frac{\sqrt{a^2-y^2}}{y})cb - 2\,\sqrt{a^2-y^2}ycb$$

$$-2\,ay\ln(\sqrt{a^2-y^2}+a)b^2 + 2\,a^2\arctan(\frac{\sqrt{b^2-y^2}}{y})cb$$

$$+2\,y\sqrt{b^2-y^2}cb + 2\,a\ln(\sqrt{b^2-y^2}+b)yb^2 + 2\,a\ln(\sqrt{b^2-y^2}+b)yc^2$$

$$-2\,cy\ln(\sqrt{b^2-y^2}+b)b^2 - 2\,c^2\arctan(\frac{\sqrt{b^2-y^2}}{y})ba - 2\,y\sqrt{b^2-y^2}ba -$$

$$2\,cy\ln(\sqrt{b^2-y^2}+b)a^2 + 2\,c\ln(\sqrt{c^2-y^2}+c)yb^2$$

$$+2\,c\ln(\sqrt{c^2-y^2}+c)ya^2 + 2\,\sqrt{c^2-y^2}yba + 2\,c^2\arctan(\frac{\sqrt{c^2-y^2}}{y})ba$$

$$-2\,ay\ln(\sqrt{a^2-y^2}+a)c^2 + \sqrt{a^2-y^2}yc^2$$

$$-4\,c\ln(\sqrt{c^2-y^2}+c)yba + 4\,ay\ln(\sqrt{a^2-y^2}+a)cb$$

$$-\sqrt{c^2-y^2}ya^2 + a^2\arctan(\frac{\sqrt{a^2-y^2}}{y})b^2 - y\sqrt{b^2-y^2}c^2 - c^2\arctan(\frac{\sqrt{c^2-y^2}}{y})a^2$$

$$-\sqrt{c^2-y^2}yb^2 + y\sqrt{b^2-y^2}a^2 + c^2\arctan(\frac{\sqrt{b^2-y^2}}{y})b^2$$

$$-a^2\arctan(\frac{\sqrt{b^2-y^2}}{y})b^2 + \sqrt{a^2-y^2}yb^2$$

$$-c^2\arctan(\frac{\sqrt{c^2-y^2}}{y})b^2 + a^2\arctan(\frac{\sqrt{a^2-y^2}}{y})c^2\Big]\ (67)$$

$$0 \le y < a\quad.$$

The second piece , $I^{II}(y)$, is

$$I^{II}(y) = \int_0^{\sqrt{b^2-y^2}} 2C_{ab}^2 dx + \int_{\sqrt{b^2-y^2}}^{\sqrt{c^2-y^2}} 2C_{bc}^2 dx$$

$$= 2\frac{b^2 {C_m}^2}{y(b^2 - 2\,ba + a^2)(c^2 - 2\,cb + b^2)} \left[y\sqrt{b^2 - y^2}c^2 + a^2 \arctan\left(\frac{\sqrt{b^2 - y^2}}{y}\right)b^2 \right.$$

$$-c^2 \arctan\left(\frac{\sqrt{b^2 - y^2}}{y}\right)b^2$$

$$-y\sqrt{b^2 - y^2}a^2 + c^2 \arctan\left(\frac{\sqrt{c^2 - y^2}}{y}\right)a^2 + c^2 \arctan\left(\frac{\sqrt{c^2 - y^2}}{y}\right)b^2 + \sqrt{c^2 - y^2}ya^2$$

$$+\sqrt{c^2 - y^2}yb^2 + 2\,a \ln(y)yb^2 + 2\,a \ln(y)yc^2 + 2\,cy \ln(\sqrt{b^2 - y^2} + b)b^2$$

$$-2\,a^2 \arctan\left(\frac{\sqrt{b^2 - y^2}}{y}\right)cb - 2\,y\sqrt{b^2 - y^2}cb - 2\,a \ln(\sqrt{b^2 - y^2} + b)yb^2$$

$$-2\,a \ln(\sqrt{b^2 - y^2} + b)yc^2 - 2\,c^2 \arctan\left(\frac{\sqrt{c^2 - y^2}}{y}\right)ba - 2\,\sqrt{c^2 - y^2}yba$$

$$-2\,c \ln(\sqrt{c^2 - y^2} + c)ya^2 - 2\,c \ln(\sqrt{c^2 - y^2} + c)yb^2 + 2\,c^2 \arctan\left(\frac{\sqrt{b^2 - y^2}}{y}\right)ba$$

$$+2\,y\sqrt{b^2 - y^2}ba + 2\,cy \ln(\sqrt{b^2 - y^2} + b)a^2 - 4\,a \ln(y)ycb + 4\,c \ln(\sqrt{c^2 - y^2} + c)yba \bigg] \quad (68)$$

$$a \le y < b \quad .$$

The third piece , $I^{III}(y)$, is

$$I^{III}(y) = \int_0^{\sqrt{c^2-y^2}} 2C_{bc}^2 dx$$

$$= 2\frac{b^2 C_m{}^2}{y\,(b^2 - 2\,ba + a^2)\,(c^2 - 2\,cb + b^2)}\Big[y\sqrt{c^2-y^2}b^2 + c^2\arctan(\frac{\sqrt{c^2-y^2}}{y})b^2$$

$$-\sqrt{a^2-y^2}yb^2 + c^2\arctan(\frac{\sqrt{c^2-y^2}}{y})a^2 + y\sqrt{c^2-y^2}a^2 - \sqrt{a^2-y^2}yc^2$$

$$+a^2\arctan(\frac{\sqrt{b^2-y^2}}{y})b^2 + \sqrt{b^2-y^2}yc^2 - \sqrt{b^2-y^2}ya^2 - c^2\arctan(\frac{\sqrt{b^2-y^2}}{y})b^2$$

$$-a^2\arctan(\frac{\sqrt{a^2-y^2}}{y})b^2 - a^2\arctan(\frac{\sqrt{a^2-y^2}}{y})c^2 + 2\,cy\ln(\sqrt{b^2-y^2}+b)a^2$$

$$+2\,ay\ln(\sqrt{a^2-y^2}+a)c^2 + 2\,a^2\arctan(\frac{\sqrt{a^2-y^2}}{y})cb - 2\,a\ln(\sqrt{b^2-y^2}+b)yc^2$$

$$-2\,a\ln(\sqrt{b^2-y^2}+b)yb^2 - 2\,\sqrt{b^2-y^2}ycb - 2\,a^2\arctan(\frac{\sqrt{b^2-y^2}}{y})cb$$

$$+2\,cy\ln(\sqrt{b^2-y^2}+b)b^2 - 2\,c\ln(\sqrt{c^2-y^2}+c)yb^2 - 2\,c\ln(\sqrt{c^2-y^2}+c)ya^2$$

$$-2\,y\sqrt{c^2-y^2}ba - 2\,c^2\arctan(\frac{\sqrt{c^2-y^2}}{y})ba + 2\,ay\ln(\sqrt{a^2-y^2}+a)b^2$$

$$+2\,\sqrt{a^2-y^2}ycb + 2\,\sqrt{b^2-y^2}yba + 2\,c^2\arctan(\frac{\sqrt{b^2-y^2}}{y})ba$$

$$+4\,c\ln(\sqrt{c^2-y^2}+c)yba - 4\,ay\ln(\sqrt{a^2-y^2}+a)cb\Big]\ (69)$$

$$b \le y < c \quad .$$

The profile of I made by the three pieces (68), (69) and (70), can be calibrated on the real data of A39 and an acceptable match is realized adopting the parameters reported in Table 10.

The theoretical intensity can therefore be plotted as a function of the distance from the center , see Figure 23, or as an image , see Figure 24.

The effect of the insertion of a threshold intensity , I_{tr}, given by the observational techniques , is now analyzed. The threshold intensity can be parametrized to I_{max}, the maximum value of intensity characterizing the ring: a typical image with a hole is visible in Figure 25 when $I_{tr} = I_{max}/2$.

The position of the minimum of I is at $y = 0$ and the position of the maximum is situated at $y = b$.

The ratio between the theoretical intensity at maximum , I_{max} at $y = b$, and at the minimum ($y = 0$) is given by

$$\frac{I_{max}}{I(y=0)} = \frac{Numerator}{Denominator} \quad , \tag{70}$$

Table 10. Simulation of the PN A39 with 3D diffusion

symbol	meaning	value
a	radius of the internal absorbing sphere	$65.96''$
b	radius of the shock	$80''$
c	radius of the external absorbing sphere	$103.5''$
R_{shell}	observed radius of the shell	$77''$
$\delta\,r_{shell}$	observed thickness of the shell	$10.1''$
$\frac{I_{limb}}{I_{center}}$	ratio of observed intensities	$(1.88 - 2.62)$
$\frac{I_{max}}{I(y=0)}$	ratio of theoretical intensities	2.84
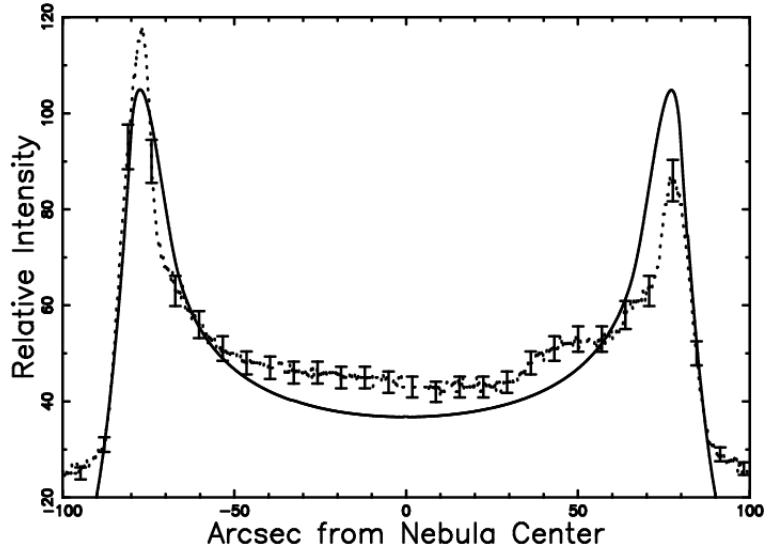
Figure 23. Cut of the mathematical intensity I (formulas (68), (69) and (70)) , crossing the center (full line) of PN A39 and real data (dotted line with some error bar). The number of data is 801 and for this model $\chi^2 = 19.03$ against $\chi^2 = 12.60$ of the rim model fully described in Jacoby et al. (2001).
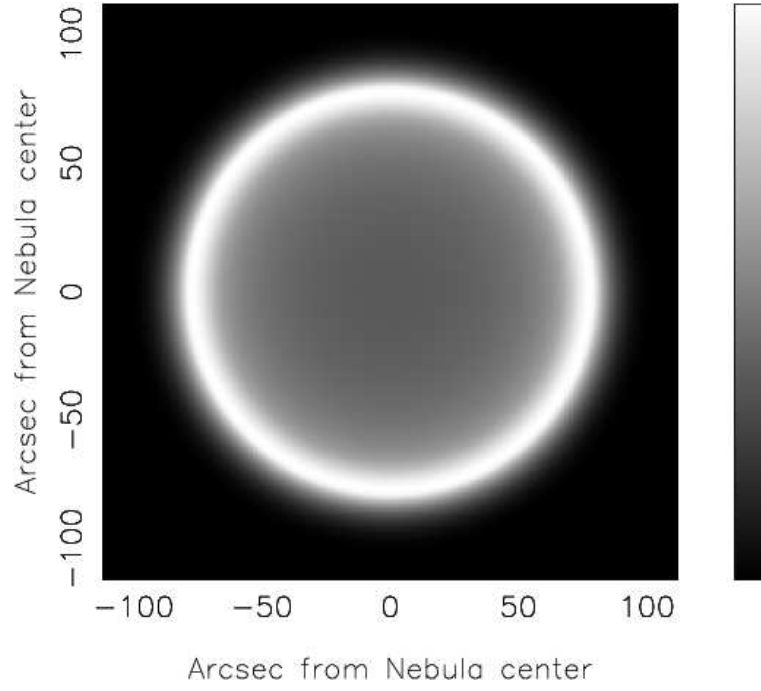
Figure 24. Contour map of I particularized to simulate the PN A39.
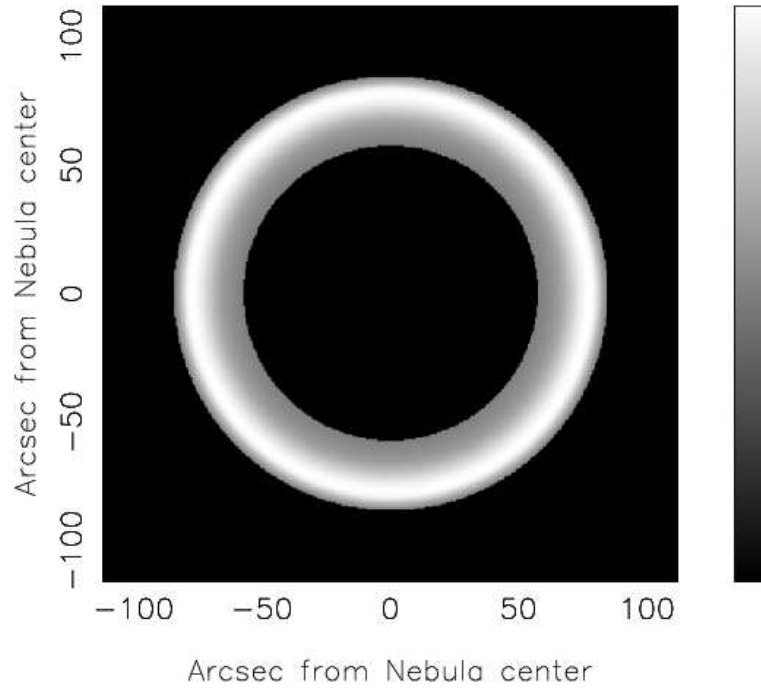
Figure 25. The same as Figure 24 but with $I_{tr} = I_{max}/2$

where

$$Numerator = (b^2 - 2\,ba + a^2)$$
$$\times (2\,cb\ln(b) - 2\,c\ln(\sqrt{c^2 - b^2} + c)b + b\sqrt{c^2 - b^2} + c^2\arctan(\frac{\sqrt{c^2 - b^2}}{b}))\quad, \quad (71)$$

and

$$Denominator = \quad (72)$$
$$2\,b(a^2c - c^2a - 2\,bca\ln(a) + 2\,bca\ln(c) - ba^2 + bc^2 - b^2c + b^2a + b^2a\ln(a)$$
$$-c^2a\ln(b) + b^2c\ln(b) - b^2a\ln(b) - b^2c\ln(c) + a^2c\ln(b) + c^2a\ln(a) - a^2c\ln(c))\quad.$$

The ratio rim(maximum) /center(minimum) of the observed intensities as well as the theoretical one are reported in Table 10 for A39 [86].

7.3.   3D diffusion from a sphere, linear dependence

The concentration rises from 0 at $r=a$ to a maximum value C_m at $r=b$ and then falls again to 0 at $r=c$. The concentrations to be used are formulas (40) and (41) once $r = \sqrt{x^2 + y^2}$ is imposed; these two concentrations are inserted in formula (52) which represents the transfer equation. The geometry of the phenomenon fixes three different zones $(0 - a, a - b, b - c)$ for the variable y, see [85, 86]; the first segment, $I^I(y)$, is

$$I^I(y) =$$
$$2\frac{bC_m\sqrt{a^2 - y^2}}{-b + a} - 2\frac{bC_m a\ln\left(\sqrt{a^2 - y^2} + a\right)}{-b + a} - 2\frac{bC_m\sqrt{b^2 - y^2}}{-b + a}$$
$$+2\frac{bC_m a\ln\left(\sqrt{b^2 - y^2} + b\right)}{-b + a} + 2\frac{bC_m c\ln\left(\sqrt{b^2 - y^2} + b\right)}{-c + b}$$
$$-2\frac{bC_m\sqrt{b^2 - y^2}}{-c + b} - 2\frac{bC_m c\ln\left(\sqrt{c^2 - y^2} + c\right)}{-c + b} + 2\frac{bC_m\sqrt{c^2 - y^2}}{-c + b} \quad (73)$$
$$0 \le y < a \quad.$$

The second segment, $I^{II}(y)$, is

$$I^{II}(y) = -\frac{bC_m a\ln\left(y^2\right)}{-b + a} - 2\frac{bC_m\sqrt{b^2 - y^2}}{-b + a}$$
$$+2\frac{bC_m a\ln\left(\sqrt{b^2 - y^2} + b\right)}{-b + a} + 2\frac{bC_m c\ln\left(\sqrt{b^2 - y^2} + b\right)}{-c + b}$$
$$-2\frac{bC_m\sqrt{b^2 - y^2}}{-c + b} - 2\frac{bC_m c\ln\left(\sqrt{c^2 - y^2} + c\right)}{-c + b} + 2\frac{bC_m\sqrt{c^2 - y^2}}{-c + b} \quad (74)$$
$$a \le y < b \quad.$$

Table 11. Simulation of the SNR SN 1993J by 3D diffusion, optically thin case

symbol	meaning	value
a	radius internal sphere	$1.76(mas)$
b	radius shock	$2.2(mas)$
c	radius external sphere	$5.0(mas)$
$\frac{I_{limb}}{I_{center}}$	ratio observed intensities	1.7926
$\frac{I_{max}}{I(y=0)}$	ratio theoretical intensities	1.7927

The third segment, $I^{III}(y)$, is

$$I^{III}(y) = \frac{bC_m c \ln\left(y^2\right)}{-c+b} - 2\frac{bC_m c \ln\left(\sqrt{c^2 - y^2} + c\right)}{-c+b} + 2\frac{bC_m \sqrt{c^2 - y^2}}{-c+b}$$
$$b \le y < c \quad . \tag{75}$$

The profile of I made up of the three segments (73), (74) and (76), can be calibrated against the real data of SN 1993J and an acceptable match can be achieved by adopting the parameters reported in Table 11. The theoretical intensity can therefore be plotted as a function of the distance from the center, see Figure 26, or as a contour map, see Figure 27.

The position of the minimum of I is at $y = 0$ and the position of the maximum is situated in the region $a \le y < b$, or more precisely at:

$$y = \frac{\sqrt{-(b - 2a + c)a(ab - 2bc + ac)}}{b - 2a + c} \quad . \tag{76}$$

This means that the maximum emission is not at the position of the shock, identified here as b, but shifted a little towards the center; see Figure 28.

The ratio between the theoretical intensity at maximum , I_{max} , as given by formula (76) and at minimum ($y = 0$) is given by

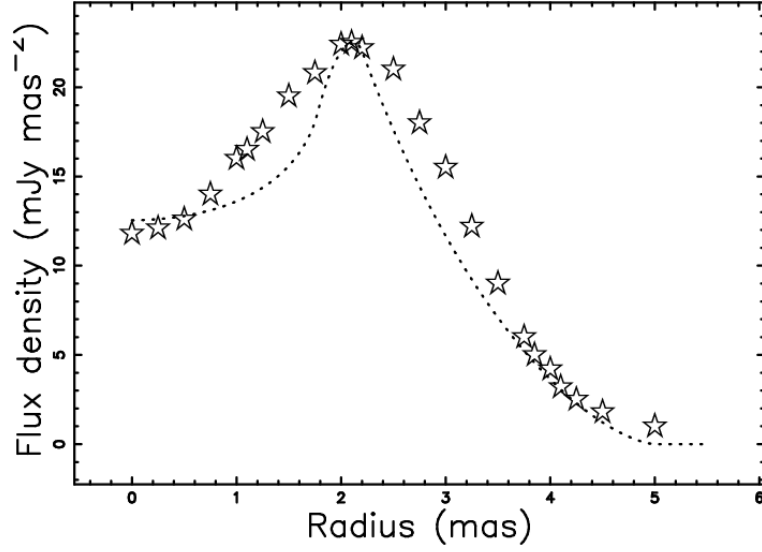$$\frac{I_{max}}{I(y = 0)} = \frac{Numerator}{Denominator} \quad , \tag{77}$$

Figure 26. Cross-section of the mathematical intensity I (formulas (73), (74) and (76)), through the center (dotted line) of SN 1993J and real data (empty stars), $\chi^2 = 100.49$ The real data made on day 1889 of SNR SN 1993J after the explosion have been extracted by the author from Figure 3 of Marcaide et al. (2009). Parameters as in Table 11.
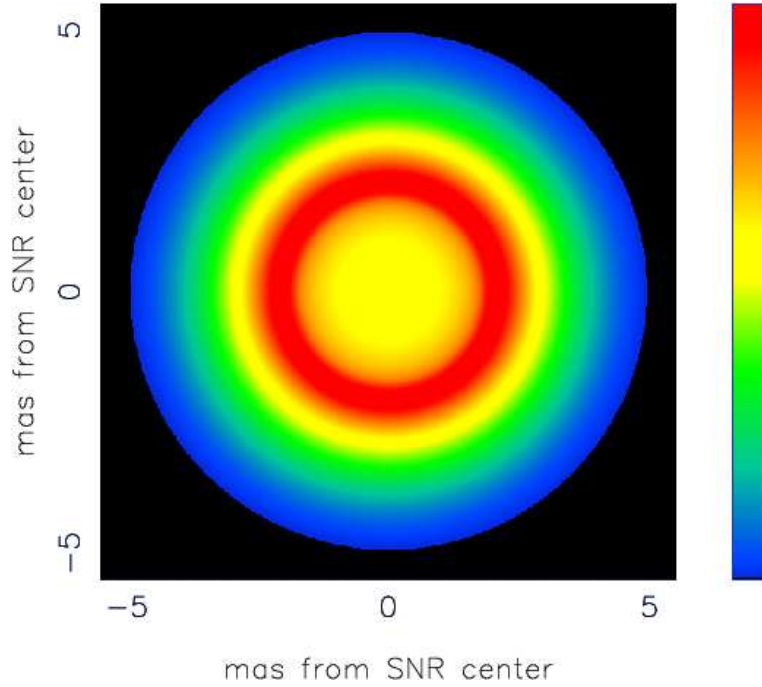

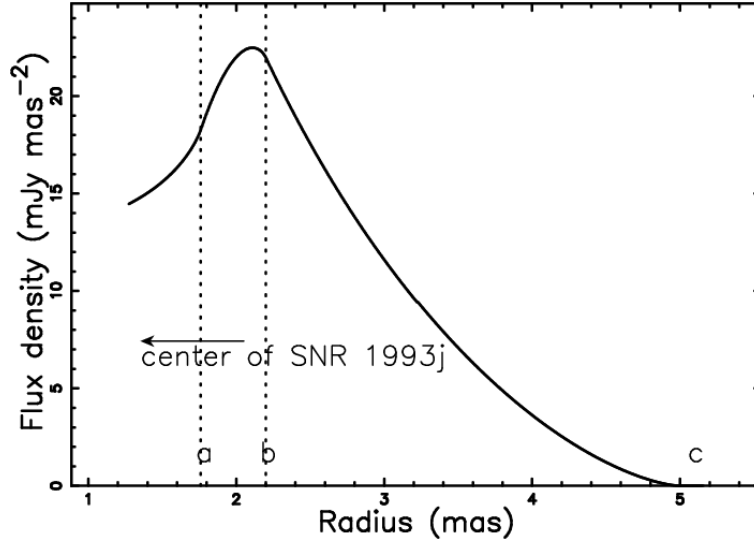Figure 27. Contour map of I adjusted to simulate the SNR SN 1993J . Parameters as in Table 11.

Figure 28. Cross-section through the mathematical intensity I towards the edge of the SNR SN 1993J . The three parameters which characterize the expanding PN, a , b and c, are reported. Parameters as in Table 11.

where

$$
\begin{aligned}
Numerator = \\
-a\ln\left(-\frac{(ac+ab-2\,cb)\,a}{b+c-2\,a}\right)c+a\ln\left(-\frac{(ac+ab-2\,cb)\,a}{b+c-2\,a}\right)b-2\sqrt{\frac{(c+b)\,(b-a)^2}{b+c-2\,a}}c \\
-2\,a\ln\left(\sqrt{\frac{(c+b)\,(b-a)^2}{b+c-2\,a}}+b\right)b+ \\
2\,c\ln\left(\sqrt{\frac{(c+b)\,(b-a)^2}{b+c-2\,a}}+b\right)b+2\sqrt{\frac{(c+b)\,(b-a)^2}{b+c-2\,a}}a \\
-2\,c\ln\left(\sqrt{\frac{(a-c)^2\,(c+b)}{b+c-2\,a}}+c\right)b+ \\
2\,c\ln\left(\sqrt{\frac{(a-c)^2\,(c+b)}{b+c-2\,a}}+c\right)a+2\sqrt{\frac{(a-c)^2\,(c+b)}{b+c-2\,a}}b- \\
2\sqrt{\frac{(a-c)^2\,(c+b)}{b+c-2\,a}}a \quad,(78)
\end{aligned}
$$
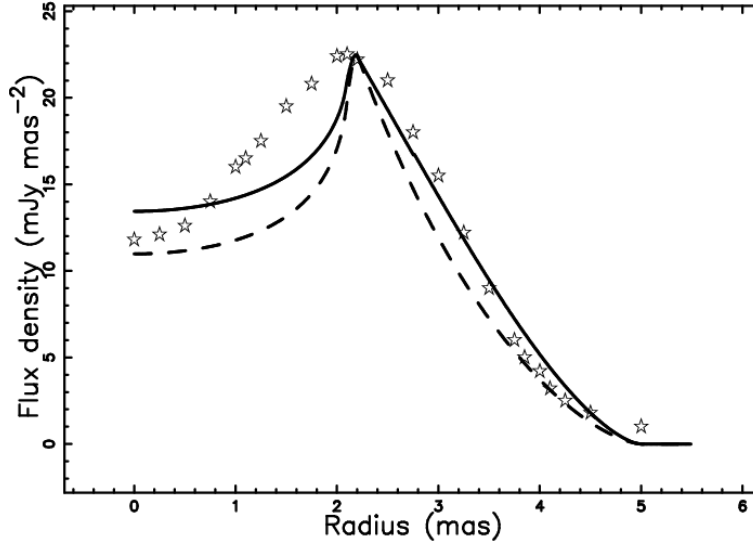
Figure 29. Cross-section through the mathematical intensity I (formulas (73), (74) and (76)), in the optically thin case (dashed line, $\chi^2 = 237.3$), and optically thick case (full line, $\chi^2 = 84.7$) and real data (empty stars) for SNR SN 1993J . Parameters as in Table 12.

and

$$Denominator =$$
$$-2\,ac\ln{(a)} + 2\,ba\ln{(a)} - 2\,ba\ln{(b)} + 2\,bc\ln{(b)} - 2\,bc\ln{(c)} + 2\,ac\ln{(c)} \quad . \quad (79)$$

The observed ratio as well as the theoretical ratio are reported in Table 11.

The effect of absorption is easily evaluated by applying formula (63) and fixing the value of K_a. The result is shown in Figure 29.

7.4. 3D complex morphologies of PN

The numerical approach to the intensity map can be implemented when the ellipsoid that characterizes the expansion surface of the PN has a constant thickness expressed , for example , as r_{min}/f where r_{min} is the minimum radius of the ellipsoid and f an integer. We remember that $f = 12$ has a physical basis in the symmetrical case , see [33]. The numerical algorithm that allows us to build the image is now outlined

- A memory grid $\mathcal{M}(i, j, k)$ that contains $NDIM^3$ pixels is considered

- The points of the thick ellipsoid are memorized on $\mathcal{M}$

- Each point of $\mathcal{M}$ has spatial coordinates x, y, z which can be represented by the following 1×3 matrix ,A,

$$A = \begin{bmatrix} x \\ y \\ z \end{bmatrix} \quad . \quad (80)$$

Table 12. Simulation of the SNR SN 1993J with 3D diffusion, optically thick case with $K_a = 0.2$.

symbol	meaning	value
a	radius internal sphere	$2.01(mas)$
b	radius of shock	$2.2(mas)$
c	radius external sphere	$5.0(mas)$
$\frac{I_{limb}}{I_{center}}$	ratio observed intensities	1.7926
$\frac{I_{max}}{I(y=0)}$	ratio optically thin case	2.0491
$\frac{I_{max}}{I(y=0)}$	ratio optically thick case	1.6741

The point of view of the observer is characterized by the Eulerian angles (Φ, Θ, Ψ) and therefore by a total rotation 3×3 matrix , E , see [67]. The matrix point is now represented by the following 1×3 matrix , B,

$$B = E \cdot A   . \tag{81}$$

- The map in intensity is obtained by summing the points of the rotated images along a direction , for example along z , (sum over the range of one index, for example k).

Figure 30 reports the rotated image of the Ring nebula and Figure 31 reports two cuts along the polar and equatorial directions.

Figure 32 reports the comparison between a theoretical and observed east-west cut in H_β that cross the center of the nebula, see Figure 1 in [87].

A comparison can be made with the color composite image of Doppler-shifted H_2 emission as represented in Figure 2 in [42].

In order to explain some of the morphologies which characterize the PN's we first map MyCn 18 with the polar axis in the vertical direction , see map in intensity in Figure 33. The vertical and horizontal cut in intensity are reported in Figure 35. The point of view of the observer as modeled by the Euler angles increases the complexity of the shapes : Figure 34 reports the after rotation image and Figure 36 the vertical and horizontal rotated cut. The after rotation image contains the double ring and an enhancement in intensity of the central region which characterize MyCn 18.

This central enhancement can be considered one of the various morphologies that the PNs present and is similar to model $BL_1 - F$ in Figure 3 of the Atlas of synthetic line profiles by [16].

7.5.   3D complex morphology of the hybrid η-Carinae

Here we adopt the numerical algorithm developed in the previous Section 7.4.. An ideal image of the Homunculus nebula having the polar axis aligned with the z-direction which means polar axis along the z-direction, is shown in Figure 37 and this should be compared
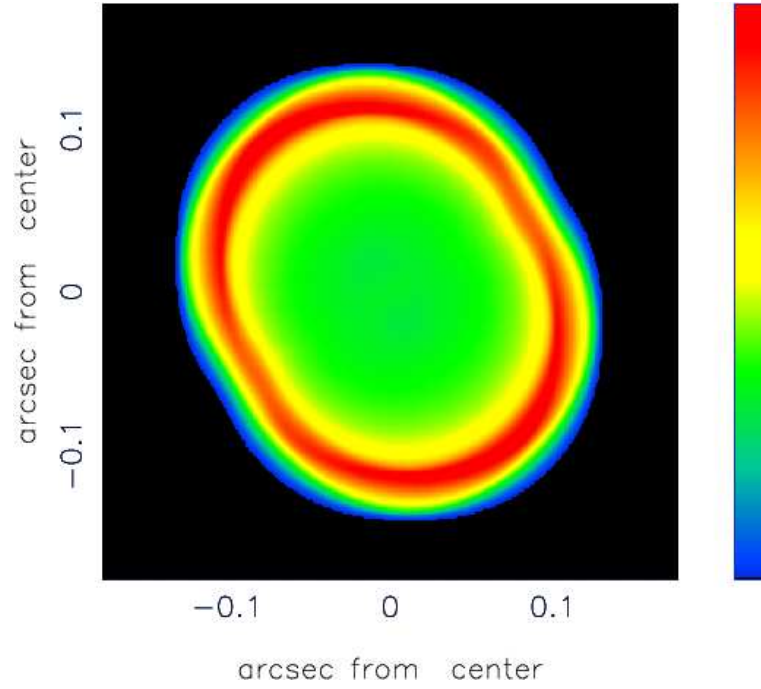
Figure 30.   Map of the theoretical intensity of the PN Ring nebula. Physical parameters as in Table 1 and f=12 . The three Eulerian angles characterizing the point of view are Φ=180 °, Θ=90 ° and Ψ=-30 °.
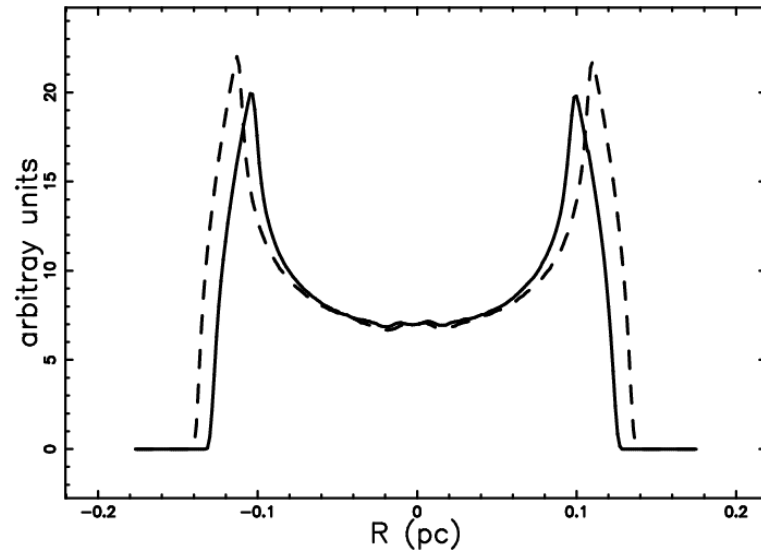

Figure 31.   Two cut of the mathematical intensity I crossing the center of the PN Ring nebula: equatorial cut (full line) and polar cut (dotted line) .
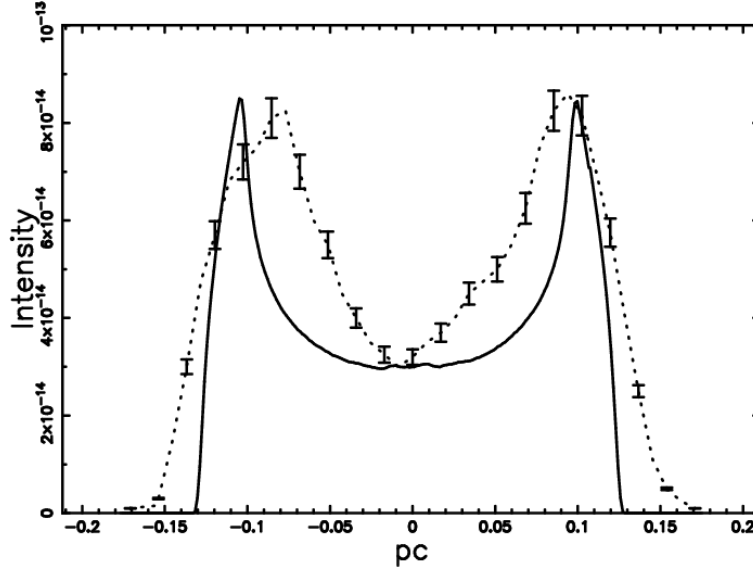
Figure 32. Cut of the mathematical intensity I of the PN Ring Nebula crossing the center (full line) and real data of H_β (dotted line with some error bar) . The number of data is 250 and for this model $\chi^2 = 15.53$. The real data are extracted by the author from Figure 1 of Garnett and Dinerstein 2001.

with the H_2 emission structure reported in Figure 4 of [55]. A model for a realistically rotated Homunculus is shown in Figure 38. This should be compared with Figure 1 in [88] or Figure 1 in [55].

The rotated image exhibits a double ring and an intensity enhancement in the central region which characterizes the little Homunculus, see [47, 48, 51, 89]. Figure 39 and Figure 40 show two cuts through the Homunculus nebula without and with rotation. The intensity enhancement is due to a projection effect and is an alternative for the theory that associates the little Homunculus with an eruption occurring some time after the Great Eruption, see [51, 89]. We briefly recall that a central enhancement is visible in one of the various morphologies characterizing planetary nebulae. This can be compared with the model $BL_1 - F$ in Figure 3 of the Atlas of synthetic line profiles by [16].

Such cuts are common when analyzing planetary nebulae. As an example Figure 4 in [40] reports a nearly symmetrical profile of the intensity in the [OIII] image of A39, a nearly spherical planetary nebula. Another example is the east-west cut in $H\beta$ for the elliptical Ring nebula, crossing the center of the nebula, see Figure 1 in [87]. Such intensity cuts are not yet available for η-Carinae and therefore can represent a new target for the observers.

7.6. 3D complex morphology of a SNR , SN 1006

The theory of an asymmetric SNR was developed in Sect. 4.1 of [68] in which an expansion surface as a function of a non-homogeneous ISM was computed: in the same paper Figure 8
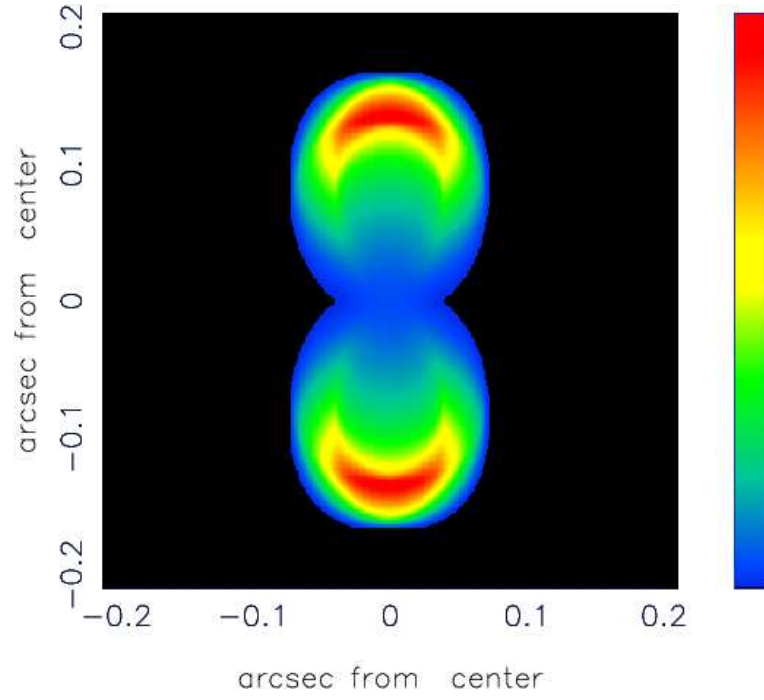
Figure 33. Map of the theoretical intensity of the PN MyCn 18 . Physical parameters as in Table 6 and f=12 . The three Eulerian angles characterizing the point of view are Φ=180 $^\circ$, Θ=90 $^\circ$ and Ψ=0 $^\circ$.
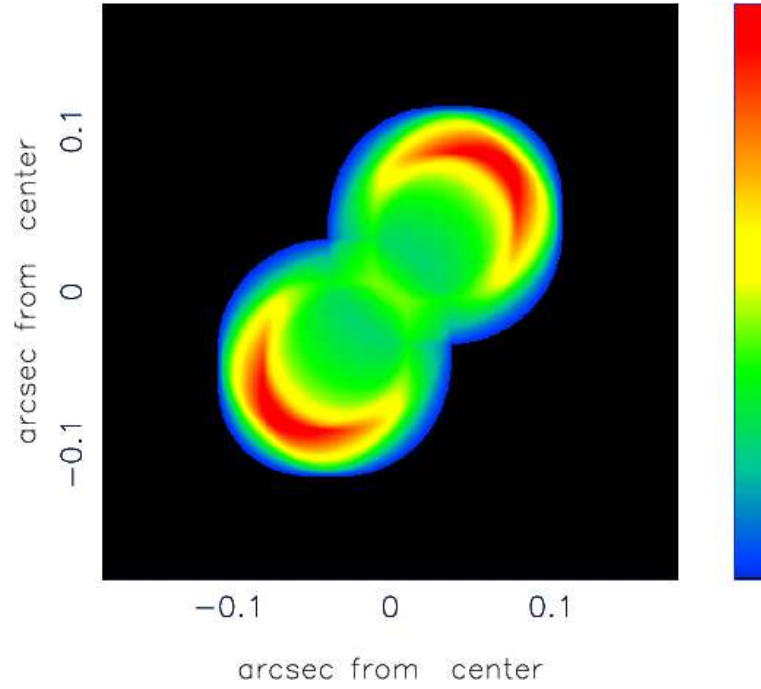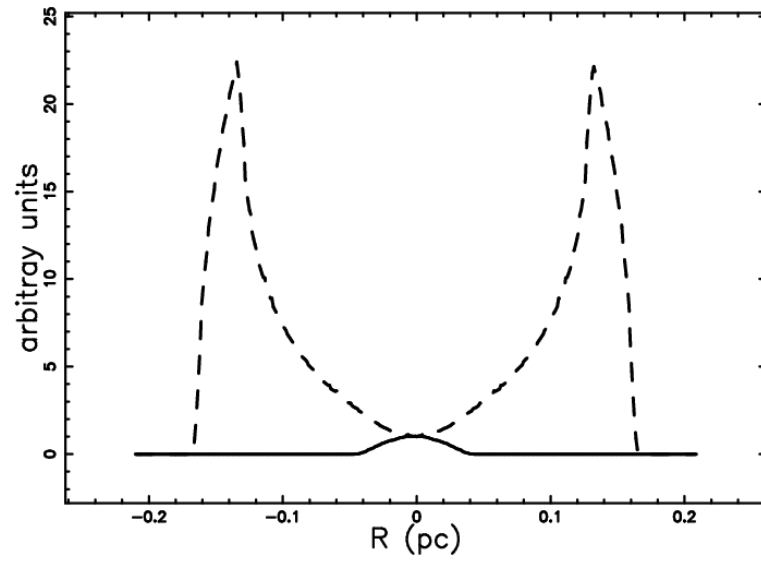
Figure 34. Map of the theoretical intensity of the rotated PN MyCn 18 . Physical parameters as in Table 6 and f=12 . The three Eulerian angles characterizing the point of view are Φ=130 $^\circ$, Θ=40 $^\circ$ and Ψ=5 $^\circ$.

Figure 35. Two cut of the mathematical intensity I crossing the center of the PN MyCn 18 : equatorial cut (full line) and polar cut (dotted line) . Parameters as in Figure 33.
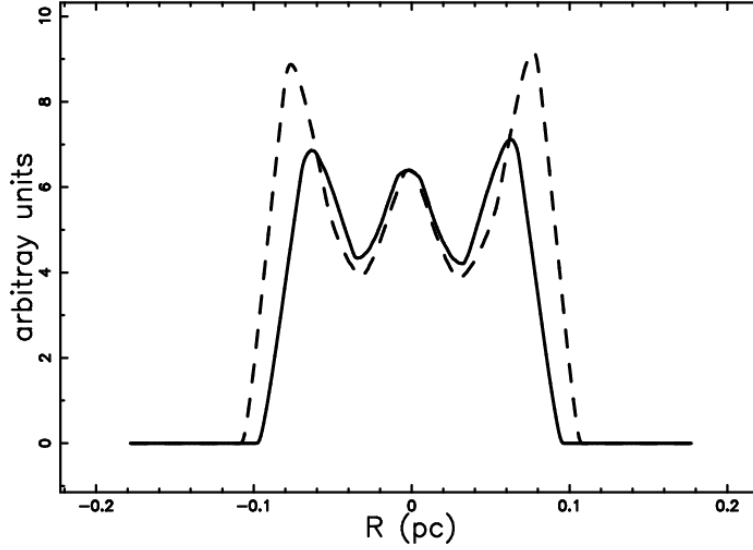
Figure 36.   Two cut of the mathematical intensity I crossing the center of the rotated PN MyCn 18 nebula: equatorial cut (full line) and polar cut (dotted line) . Parameters as in Figure 34.

models SN1006. The diffusing algorithm adopted here is the 3D random walk from many injection points (in the following IP)

1. The first IP is chosen

2. The first of the NPART electrons is chosen.

3. The random walk of an electron starts where the selected IP is situated. The electron moves in one of the six possible directions.

4. After N steps the process restarts from (2)

5. The number of visits is recorded on $\mathcal{M}^3$, a three–dimensional grid.

6. The random walk terminates when all the NPART electrons are processed.

7. The process restarts from (1) selecting another IP

8. For the sake of normalization the one–dimensional visitation/concentration grid $\mathcal{M}^3$ is divided by NPART.

The *IP* are randomly selected in space, and the radius is computed by using the method of bilinear interpolation on the four grid points that surround the selected latitude and longitude, ([66]). The radius will be the selected value + *R*/24 in order to generate the IP where the action of the shock is maximum.

Our model gives radial velocities , V_{theo} , $2211\ km\ s^{-1} \leq\ V_{theo}\ \leq 3580\ km\ s^{-1}$ and the map of the expansion velocity is reported in Figure 41 from which it is possible to
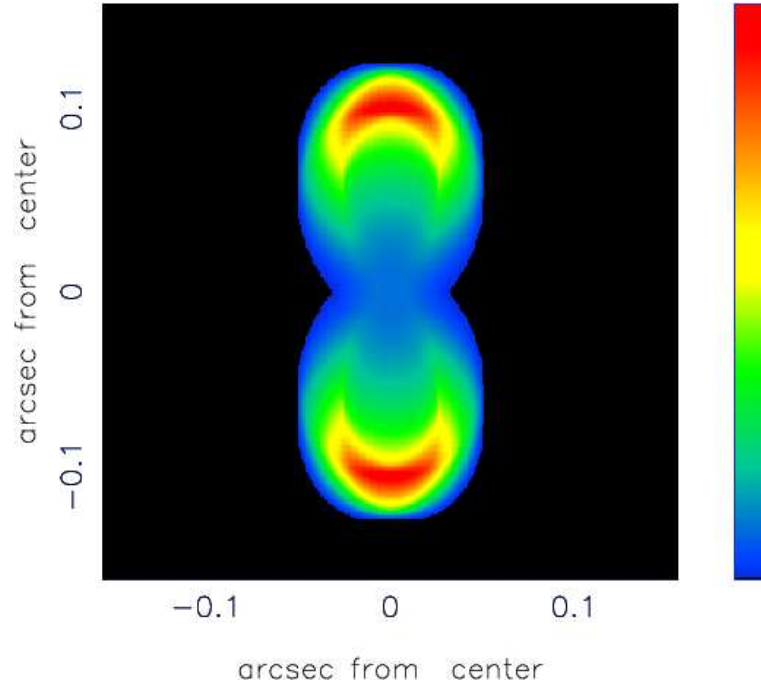
Figure 37.   Map of the theoretical intensity of the hybrid Homunculus/η-Carinae nebula in the presence of an exponentially varying medium. Physical parameters as in Table 6. The three Euler angles characterizing the orientation are Φ=180°, Θ=90° and Ψ=0°. This combination of Euler angles corresponds to the rotated image with the polar axis along the z-axis.
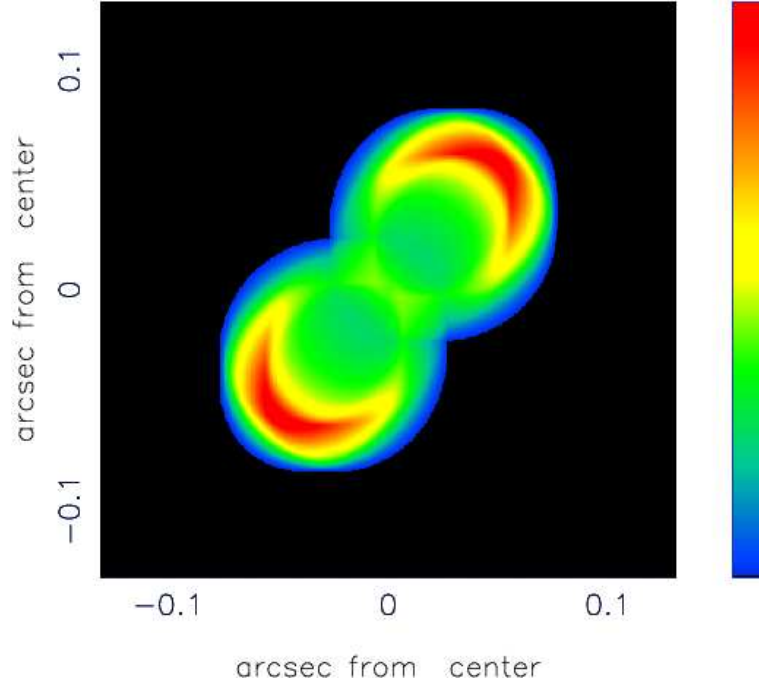
Figure 38. Model map of the of the hybrid Homunculus/η-Carinae nebula rotated in accordance with the observations, for an exponentially varying medium. Physical parameters as in Table 6. The three Euler angles characterizing the orientation of the observer are Φ=130°, Θ=40° and Ψ=-140°. This combination of Euler angles corresponds to the observed image.
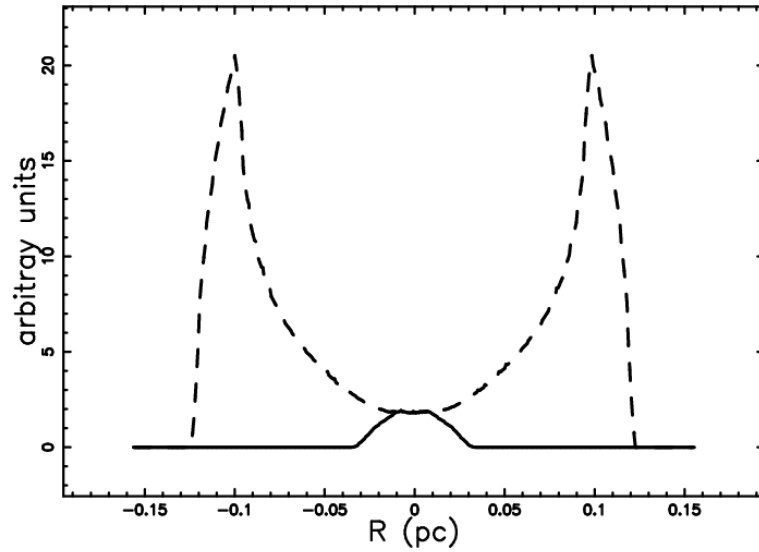

Figure 39. Two cuts of the model intensity across the center of the hybrid Homunculus/η-Carinae nebula for an exponentially varying medium: equatorial cut (full line) and polar cut (dotted line). Parameters as in Figure 37.
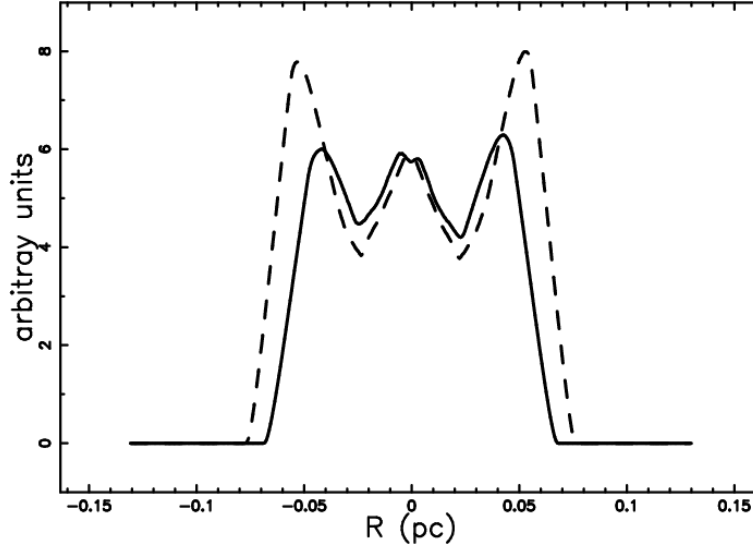
Figure 40.　　Two cuts of the model intensity across the center of the realistically rotated hybrid Homunculus/$\eta - car$ nebula for an exponentially varying medium: equatorial cut (full line) and polar cut (dotted line). Parameters as in Figure 38.

visualize the differences in the expansion velocities among the various regions as well as the overall elliptical shape.

Before continuing we should recall that in the presence of discrete time steps on a 3D lattice the average square radius ,$\langle R^2(N)\rangle$, after N steps (see [90], equation (12.5)) is

$$\langle R^2(N)\rangle \sim 6DN \quad , \tag{82}$$

from which the diffusion coefficient , D , is derived

$$D = \frac{\langle R^2(N)\rangle}{6N} \quad . \tag{83}$$

The two boundaries in which the random walk is taking place are now represented by two irregular surfaces. It is possible to simulate them by stopping the random walk after a number of iterations N given by

$$N = NINT(\frac{\overline{R}_{pc}}{24}\frac{1}{\delta})^2 \quad , \tag{84}$$

where $\overline{R}_{pc}$ represents the averaged radius in pc . These are the iterations after which according, to formula (83), the walkers reach the boundaries at a radial distance given by $\frac{\overline{R}_{pc}}{24}$ from the place of injection; in other words we are working on an unbounded lattice . The influence of velocity on the flux F of radiation can be inferred from the suspected dependence when non-thermal emission is considered, see equation (9.29) in [91],

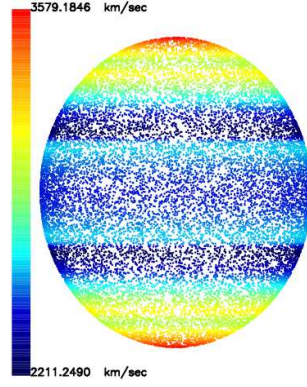$$F = \chi_t\frac{1}{4}\mu_H n_0 v_s^3 \quad , \tag{85}$$

Figure 41. Map of the expansion velocity relative to the simulation of SNR SN 1006 when 190000 random points are selected on the surface. The physical parameters are the same as in Figure 8 of [68].

where χ_T represents the efficiency of conversion of the unitarian flux of kinetic energy, μ_H the mass of the hydrogen nucleus, n_0 the particles/cm^3 and v_s the velocity of the shock.

Assuming that the flux reversed in the non–thermal emission follows a similar law through the parameter χ_X (the efficiency in the X–region) the effect of velocity is simulated through the following algorithm. Once the IP are spatially generated, the number of times NTIMES over which to repeat the cycle is given by

$$NTIMES = 1 + NTIMES_{MAX} * (\frac{v - v_{min}}{v_{max} - v_{min}})^3 \quad , \tag{86}$$

where $NTIMES_{MAX}$ is the maximum of the allowed values of NTIMES minus 1, and v is the velocity associated to each IP. The asymmetric contour map obtained when the spatial step is $\approx$ 2 * gyro–radius is reported in Figure 42 and the cut along two perpendicular lines of the projection grid in Figure 43.

In Figure 43 the asymmetry both in the peak to peak distance and the difference in the two maximum is evident. The ratio between the X-ray emission in the bright limbs (NE or SW) and toward the northwest or southeast (at 2 keV) is around 10 , see Figure 5 top right in [92]. Conversely our theoretical ratio , see Figure 43, is 9.84. It is also possible to plot the maximum of the theoretical intensity as function of the position angle , see Figure 44. The reader can make a comparison with the observational counterpart represented by Figure 5 top right, dashed line in [92].

8. Conclusions

Law of motion The law of motion in the case of a symmetric motion can be modeled by a power law solution , the Sedov Solution or the radial momentum conservation. These three models allow to determine the approximate age of A39 which is 8710 yr for the Sedov solution and 50000 yr for the radial momentum conservation. In presence of gradients as given , for example , by an exponential behavior, the solution is deduced through the
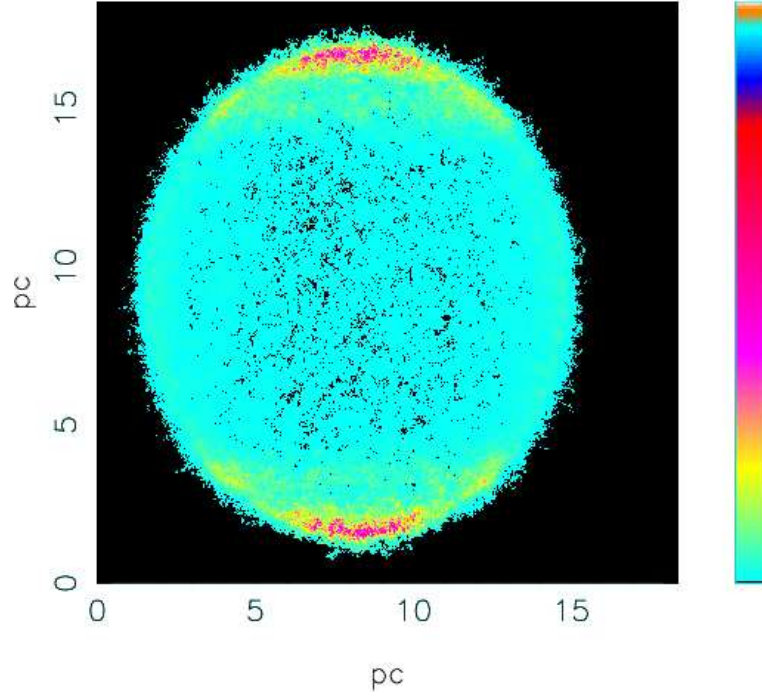
Figure 42.   Contour of the intensity *I* in the X-rays of SNR SN 1006 . The parameters are $side_{SNR}$=18.37 pc , $\delta = 6.12\ 10^{-3}$ pc, $\rho = 2.8\ 10^{-3}$ pc, NDIM=3001, $IP = 190000^2$, *NPART= 100*, $NTIMES_{max}$=18, great box. Optically thin layer.
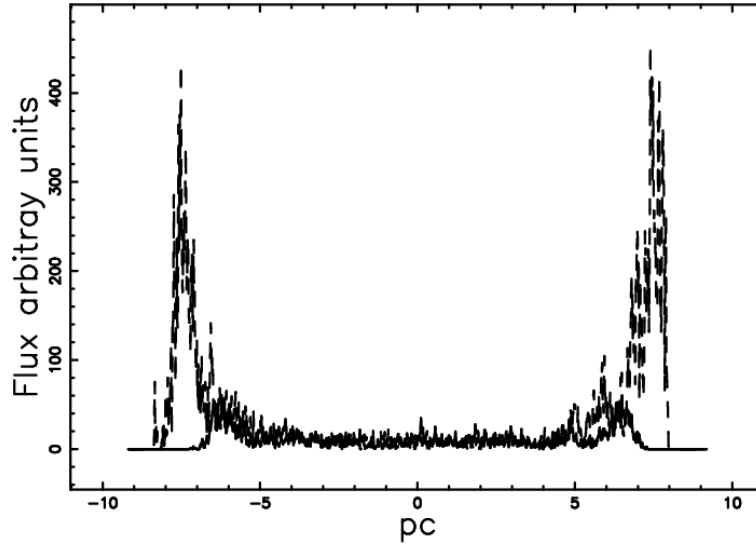

Figure 43.   Two cut along perpendicular lines of *I* for SNR SN 1006 reported in Figure 42 . Optically thin layer.
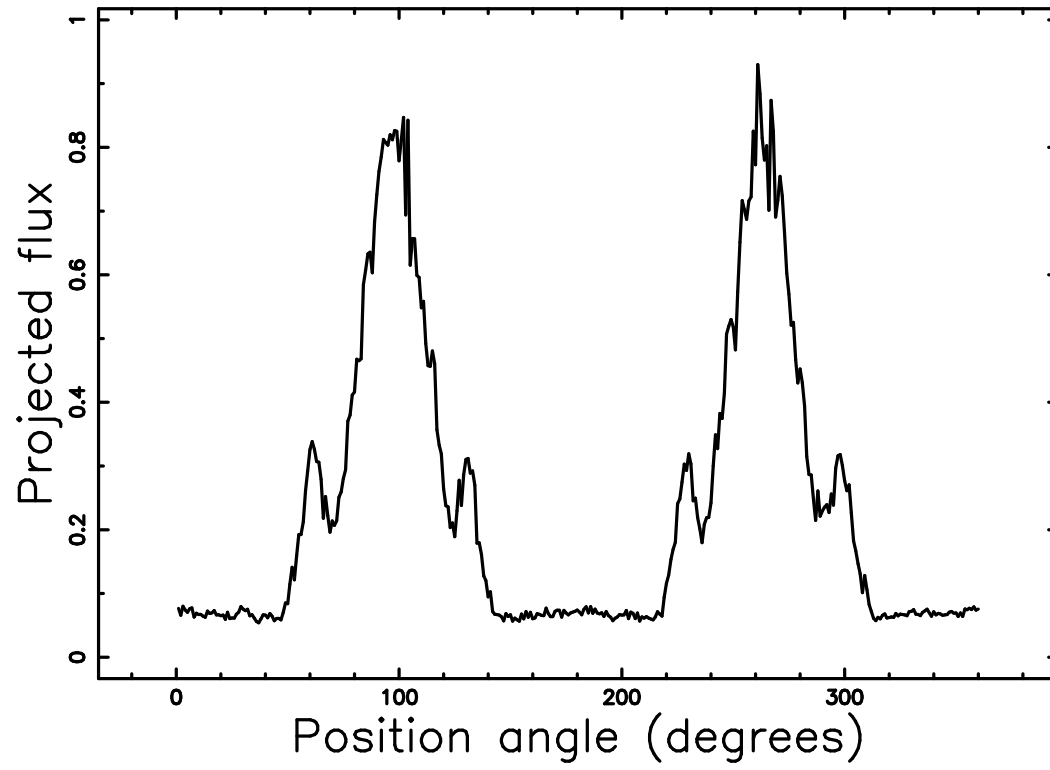
Figure 44.   Azimuthal maximum of the profiles of intensity as function of the position angle in degrees for SNR SN 1006 . Same parameters as in Figure 42.

radial momentum conservation. The comparison with the astronomical data is now more complicated and the single and multiple efficiency in the radius determination have been introduced. When , for example , MyCn 18 is considered , the multiple efficiency over 18 directions is 90.66% when the age of 2000 yr is adopted. In the case of η-Carinae the multiple efficiency over 18 directions is 85% for a fixed age of 158 yr in an exponentially varying medium. In the case of the weakly asymmetric SN 1006 the efficiency is 94.9% in the polar direction and 92.5% in the equatorial direction for a fixed age of 974 yr in an exponentially varying medium.

Diffusion

The number density in a thick layer surrounding the ellipsoid of expansion can be considered constant or variable from a maximum value to a minimum value with the growing or diminishing radius in respect to the expansion position. In the case of a variable number density the framework of the mathematical diffusion has been adopted, see formulas (40) and (41). The case of diffusion with drift has been analytically solved , see formulas (45) and (46), and the theoretical formulas have been compared with values generated by Monte Carlo simulations.

Formation of the image

The intensity of the image of a symmetrical PN or SNR in the case of optically thin medium can be computed through an analytical evaluation of lines of sight when the number density is constant between two spheres see formula (65). The case of a symmetrical diffusive process which is built in presence of three spheres we should distinguish between

- intensity of emission proportional to the square of the number density corresponding to the case of PN , see formulas (68), (69) and (70).

- intensity of emission proportional to the number density corresponding to the case of SNR, see formulas (73), (74) and (76).

In the case of complex morphologies assuming an optically thin medium, it is possible to make a model image once two hypotheses are made:

1. The thickness of the emitting layer, ΔR, is the same everywhere $\Delta R = 0.03R_{max}$, where R_{max} is the maximum radius of expansion.

2. The density of the emitting layer is constant everywhere

A 2D image of the PNs Ring nebula and MyCn 18 , the hybrid Homunculus/η-Carinae nebula and the weakly asymmetric SNR SN 1006 are shown respectively in Figures 30, 33, 37 and 42.

References

[1] S. Kwok, C. R. Purton, P. M. Fitzgerald, ApJ 219 (1978) L125–L127.

[2] F. Sabbadin, R. G. Gratton, A. Bianchini, S. Ortolani, A&A 136 (1984) 181–192.

[3] B. Balick, AJ 94 (1987) 671–678.

[4] H. E. Schwarz, R. L. M. Corradi, J. Melnick, A&AS 96 (1992) 23–113.

[5] A. Manchado, L. Stanghellini, M. A. Guerrero, ApJ 466 (1996) L95+.

[6] M. A. Guerrero, E. G. Jaxon, Y.-H. Chu, AJ 128 (2004) 1705–1710.

[7] N. Soker, R. Hadar, MNRAS 331 (2002) 731–735.

[8] N. Soker, MNRAS 330 (2002) 481–486.

[9] V. Icke, A&A 202 (1988) 177–188.

[10] A. Frank, B. Balick, K. Davidson, ApJ 441 (1995) L77–L80.

[11] N. Langer, G. García-Segura, M.-M. Mac Low, ApJ 520 (1999) L49–L53.

[12] R. F. González, E. M. de Gouveia Dal Pino, A. C. Raga, P. F. Velazquez, ApJ 600 (2004) L59–L62.

[13] F. D. Kahn, K. A. West, MNRAS 212 (1985) 837–850.

[14] G. Mellema, F. Eulderink, V. Icke, A&A 252 (1991) 718–732.

[15] K. H. Tsui, A&A 482 (2008) 793–802.

[16] C. Morisset, G. Stasinska, Revista Mexicana de Astronomia y Astrofisica 44 (2008) 171–180.

[17] H. Matsumoto, T. Fukue, H. Kamaya, PASJ 58 (2006) 861–868.

[18] A. D. Thackeray, The Observatory 69 (1949) 31–33.

[19] E. Gaviola, ApJ 111 (1950) 408–+.

[20] N. Smith, ArXiv e-prints .

[21] A. Nota, M. Livio, M. Clampin, R. Schulte-Ladbeck, ApJ 448 (1995) 788–+.

[22] V. V. Dwarkadas, B. Balick, AJ 116 (1998) 829–839.

[23] V. V. Dwarkadas, S. P. Owocki, ApJ 581 (2002) 1337–1343.

[24] N. Soker, ApJ 612 (2004) 1060–1064.

[25] N. Soker, ApJ 661 (2007) 490–495.

[26] R. F. González, E. M. de Gouveia Dal Pino, A. C. Raga, P. F. Velazquez, ApJ 600 (2004) L59–L62.

[27] N. Smith, R. H. D. Townsend, ApJ 666 (2007) 967–975.

[28] E. R. Parkin, J. M. Pittard, M. F. Corcoran, K. Hamaguchi, I. R. Stevens, MNRAS 394 (2009) 1758–1774.

[29] R. F. González, A. M. Villa, G. C. Gómez, E. M. de Gouveia Dal Pino, A. C. Raga, J. Cantó, P. F. Velázquez, E. de La Fuente, MNRAS 402 (2010) 1141–1148.

[30] J. H. Oort, MNRAS 106 (1946) 159–+.

[31] L. I. Sedov, Similarity and Dimensional Methods in Mechanics, Academic Press, New York, 1959.

[32] Dyson, J. E. and Williams, D. A., The physics of the interstellar medium, Institute of Physics Publishing, Bristol, 1997.

[33] A. McCray, R. In: Dalgarno, D. Layzer (Eds.), Spectroscopy of astrophysical plasmas, Cambridge University Press, Cambridge, 1987.

[34] R. A. Chevalier, ApJ 258 (1982) 790–797.

[35] R. A. Chevalier, ApJ 259 (1982) 302–310.

[36] J. K. Truelove, C. F. McKee, ApJS 120 (1999) 299–326.

[37] J. M. Marcaide, I. Martí-Vidal, A. Alberdi, M. A. Pérez-Torres, A&A 505 (2009) 927–945.

[38] I. Martí-Vidal, J. M. Marcaide, A. Alberdi, J. C. Guirado, M. A. Pérez-Torres, E. Ros, A&A 526 (2011) A142+.

[39] I. Martí-Vidal, J. M. Marcaide, A. Alberdi, J. C. Guirado, M. A. Pérez-Torres, E. Ros, A&A 526 (2011) A143+.

[40] G. H. Jacoby, G. J. Ferland, K. T. Korista, ApJ 560 (2001) 272–286.

[41] H. Hippelein, R. Weinberger, A&A 232 (1990) 129–134.

[42] D. Hiriart, PASP 116 (2004) 1135–1142.

[43] H. C. Harris, C. C. Dahn, D. G. Monet, J. R. Pier, Trigonometric parallaxes of Planetary Nebulae (Invited Review), in: H. J. Habing, H. J. G. L. M. Lamers (Eds.), Planetary Nebulae, Vol. 180 of IAU Symposium, 1997, pp. 40–+.

[44] R. L. M. Corradi, H. E. Schwarz, A&A 278 (1993) 247–254.

[45] R. Sahai, A. Dayal, A. M. Watson, J. T. Trauger, K. R. Stapelfeldt, C. J. Burrows, J. S. Gallagher, III, P. A. Scowen, J. J. Hester, R. W. Evans, G. E. Ballester, J. T. Clarke, D. Crisp, R. E. Griffiths, J. G. Hoessel, J. A. Holtzman, J. Krist, J. R. Mould, AJ 118 (1999) 468–476.

[46] A. Dayal, R. Sahai, A. M. Watson, J. T. Trauger, C. J. Burrows, K. R. Stapelfeldt, J. S. Gallagher, III, AJ 119 (2000) 315–322.

[47] N. Smith , MNRAS 337 (2002) 1252–1268.

[48] R. F. González, G. Montes, J. Cantó, L. Loinard, MNRAS 373 (2006) 391–396.

[49] N. Smith, J. A. Morse, T. R. Gull, D. J. Hillier, R. D. Gehrz, N. R. Walborn, M. Bautista, N. R. Collins, M. F. Corcoran, A. Damineli, F. Hamann, H. Hartman, S. Johansson, O. Stahl, K. Weis, ApJ 605 (2004) 405–424.

[50] M. F. Corcoran, K. Hamaguchi, T. Gull, K. Davidson, ApJ 613 (2004) 381–386.

[51] N. Smith, MNRAS 357 (2005) 1330–1336.

[52] N. Smith, K. J. Brooks, B. S. Koribalski, J. Bally, ApJ 645 (2006) L41–L44.

[53] M. Teodoro, A. Damineli, R. G. Sharp, J. H. Groh, C. L. Barbosa, MNRAS 387 (2008) 564–576.

[54] M. A. Bautista, C. Ballance, T. R. Gull, H. Hartman, K. Lodders, M. Martínez, M. Meléndez, MNRAS 393 (2009) 1503–1512.

[55] N. Smith, ApJ 644 (2006) 1151–1163.

[56] J. Ripero, F. Garcia, D. Rodriguez, P. Pujol, A. V. Filippenko, R. R. Treffers, Y. Paik, M. Davis, D. Schlegel, F. D. A. Hartwick, D. D. Balam, D. Zurek, R. M. Robb, P. Garnavich, B. A. Hong, IAU circ. 5731 (1993) 1–+.

[57] W. L. Freedman, S. M. Hughes, B. F. Madore, J. R. Mould, M. G. Lee, ApJ 427 (1994) 628–655.

[58] C. Fransson, P. M. Challis, R. A. Chevalier, A. V. Filippenko, R. P. Kirshner, ApJ 622 (2005) 991–1007.

[59] R. G. Strom, MNRAS 230 (1988) 331–344.

[60] S. P. Reynolds, D. M. Gilmore, AJ 92 (1986) 1138–1144.

[61] A. Bamba, R. Yamazaki, M. Ueno, K. Koyama, ApJ 589 (2003) 827–837.

[62] D. C. Ellison, S. P. Reynolds, K. Borkowski, R. Chevalier, D. P. Cox, J. R. Dickel, R. Pisarski, J. Raymond, S. R. Spangler, H. J. Volk, J. P. Wefel, PASP 106 (1994) 780–797.

[63] J. Vink, High Resolution X-ray Spectroscopy of SN 1006, in: R. Smith (Ed.), X-ray Diagnostics of Astrophysical Plasmas: Theory, Experiment, and Observation, Vol. 774 of American Institute of Physics Conference Series, 2005, pp. 241–251.

[64] M. Steffen, D. Schönberner, A. Warmuth, A&A 489 (2008) 173–194.

[65] P. Padmanabhan, Theoretical astrophysics. Vol. II: Stars and Stellar Systems, Cambridge University Press, Cambridge, MA, 2001.

[66] W. H. Press, S. A. Teukolsky, W. T. Vetterling, B. P. Flannery, Numerical recipes in FORTRAN. The art of scientific computing, Cambridge University Press, Cambridge, 1992.

[67] H. Goldstein, C. Poole, J. Safko, Classical mechanics, Addison-Wesley, San Francisco, 2002.

[68] L. Zaninetti, A&A 356 (2000) 1023–1030.

[69] J. Kim, J. Franco, S. S. Hong, A. Santillán, M. A. Martos, ApJ 531 (2000) 873–882.

[70] H. C. Berg, Random Walks in Biology, Princeton University Press, Princeton, 1993.

[71] J. Crank, Mathematics of Diffusion, Oxford University Press, Oxford, 1979.

[72] G. Rybicki, A. Lightman, Radiative Processes in Astrophysics, Wiley-Interscience, New-York, 1991.

[73] Hjellming, R. M., Radio stars IN Galactic and Extragalactic Radio Astronomy , Springer-Verlag, New York, 1988.

[74] K. R. Lang, Astrophysical formulae. (Third Edition), Springer, New York, 1999.

[75] P. F. Velázquez, J. J. Martinell, A. C. Raga, E. B. Giacani, ApJ 601 (2004) 885–895.

[76] E. G. Berezhko, H. J. Völk, A&A 427 (2004) 525–536.

[77] A. Bamba, R. Yamazaki, J. S. Hiraga, ApJ 632 (2005) 294–301.

[78] G. Cassam-Chenaï, A. Decourchelle, J. Ballet, D. C. Ellison, A&A 443 (2005) 955–959.

[79] A. M. Bykov, Y. A. Uvarov, D. C. Ellison, ApJ 689 (2008) L133–L136.

[80] S. Katsuda, R. Petre, K. Mori, S. P. Reynolds, K. S. Long, P. F. Winkler, H. Tsunemi, ApJ 723 (2010) 383–392.

[81] M. Cohen, J. M. Chapman, R. M. Deacon, R. J. Sault, Q. A. Parker, A. J. Green, MNRAS 369 (2006) 189–196.

[82] K. P. M. Blagrave, P. G. Martin, J. A. Baldwin, ApJ 644 (2006) 1006–1027.

[83] H. E. Schwarz, H. Monteiro, ApJ 648 (2006) 430–434.

[84] R. Gruenwald, A. Aleman, A&A 461 (2007) 1019–1025.

[85] L. Zaninetti, Baltic Astronomy 16 (2007) 251–285.

[86] L. Zaninetti, MNRAS 395 (2009) 667–691.

[87] D. R. Garnett, H. L. Dinerstein, ApJ 558 (2001) 145–156.

[88] N. Smith, R. D. Gehrz, ApJ 529 (2000) L99–L102.

[89] K. Ishibashi, T. R. Gull, K. Davidson, N. Smith, T. Lanz, AJ 125 (2003) 3222–3236.

[90] H. Gould, J. Tobochnik, An introduction to computer simulation methods, Addison-Wesley, Reading, Menlo Park, 1988.

[91] C. F. McKee, Astrophysical shocks in diffuse gas, in: A. Dalgarno, D. Layzer (Eds.), Spectroscopy of Astrophysical Plasmas, 1987, pp. 226–254.

[92] R. Rothenflug, J. Ballet, G. Dubner, E. Giacani, A. Decourchelle, P. Ferrando, A&A 425 (2004) 121–131.